JEM Journal of Experimental Medicine

ARTICLE

Immunomolecular and reactivity landscapes of gut IgA subclasses in homeostasis and inflammatory bowel disease

Sonia Tejedor Vaquero[1*], Hadas Neuman[2*], Laura Comerma[1,5], Xavi Marcos-Fa[1], Celia Corral-Vazquez[1], Mathieu Uzzan[3], Marc Pybus[1], Daniel Segura-Garzón[1], Joana Guerra[1], Lisa Perruzza[4], Roser Tachó-Piñot[1], Jordi Sintes[1], Adam Rosenstein[3], Emilie K. Grasset[3], Mar Iglesias[5], Monica Gonzalez Farré[5], Joan Lop[5], Maria Evangelina Patriaca-Amiano[5], Monica Larrubia-Loring[5], Pablo Santiago-Diaz[5], Júlia Perera-Bel[1], Pau Berenguer-Molins[1], Monica Martinez Gallo[6], Andrea Martin-Nalda[7], Encarna Varela[8,9], Marta Garrido-Pontnou[10], Fabio Grassi[4], Francisco Guarner[8,9], Saurabh Mehandru[3], Lucia Márquez-Mosquera[11], Ramit Mehr[2**], Andrea Cerutti[1,3,12**], and Giuliana Magri[1**]

The human gut includes plasma cells (PCs) expressing immunoglobulin A1 (IgA1) or IgA2, two structurally distinct IgA subclasses with elusive regulation, function, and reactivity. We show here that intestinal IgA1$^+$ and IgA2$^+$ PCs co-emerged early in life, comparably accumulated somatic mutations, and were enriched within short-lived CD19$^+$ and long-lived CD19$^-$ PC subsets, respectively. IgA2$^+$ PCs were extensively clonally related to IgA1$^+$ PCs and a subset of them presumably emerged from IgA1$^+$ precursors. Of note, secretory IgA1 (SIgA1) and SIgA2 dually coated a large fraction of mucus-embedded bacteria, including *Akkermansia muciniphila*. Disruption of homeostasis by inflammatory bowel disease (IBD) was associated with an increase in actively proliferating IgA1$^+$ plasmablasts, a depletion in long-lived IgA2$^+$ PCs, and increased SIgA1$^+$SIgA2$^+$ gut microbiota. Such increase featured enhanced IgA1 reactivity to pathobionts, including *Escherichia coli*, combined with depletion of beneficial *A. muciniphila*. Thus, gut IgA1 and IgA2 emerge from clonally related PCs and show unique changes in both frequency and reactivity in IBD.

Introduction

Human but not mouse immunoglobulin A (IgA) encompasses IgA1 and IgA2 subclasses encoded by the Cα1 and Cα2 genes, located in the first and second duplication units of the Ig heavy chain locus, respectively (Cerutti, 2008). Compared to IgA1, the IgA2 protein is less susceptible to bacterial proteolysis due to its shorter hinge region, has a distinct glycosylation pattern, and further differs from IgA1 in that it is more abundant in mucosal surfaces but scarce in the peripheral compartment, which mostly includes IgA1 (Cerutti, 2008).

Systemic plasma cells (PCs) release IgA1 as monomers, whereas mucosal PCs secrete IgA1 or IgA2 as dimers, which include a PC-derived protein called the joining (J) chain (Chen et al., 2020; Brandtzaeg et al., 1999). By binding the J chain, the polymeric Ig receptor (pIgR) from the basolateral membrane of

[1]Translational Clinical Research Program, Hospital del Mar Research Institute, Barcelona, Spain; [2]Computational Immunology Laboratory, The Mina and Everard Goodman Faculty of Life Sciences, Bar-Ilan University, Ramat-Gan, Israel; [3]Department of Medicine, Icahn School of Medicine at Mount Sinai, Immunology Institute, New York, NY, USA; [4]Institute for Research in Biomedicine, Faculty of Biomedical Sciences, Università della Svizzera Italiana, Bellinzona, Switzerland; [5]Pathology Department, Hospital del Mar, Barcelona, Spain; [6]Immunology Division, Vall d'Hebron University Hospital and Translational Immunology Research Group, Vall d'Hebron Research Institute (VHIR), Department of Cell Biology, Physiology and Immunology, Autonomous University of Barcelona (UAB), Barcelona, Spain; [7]Pediatric Infectious Diseases and Immunodeficiencies Unit, Vall d'Hebron University Hospital, Jeffrey Modell Diagnostic and Research Center for Primary Immunodeficiencies, Barcelona, Spain; [8]Department of Gastroenterology, Vall d'Hebron Research Institute, Barcelona, Spain; [9]Biomedical Research Networking Center in Hepatic and Digestive Diseases, Instituto Carlos III, Madrid, Spain; [10]Pathology Department, Hospital Universitari Vall d'Hebron, Barcelona, Spain; [11]Department of Gastroenterology, Hospital del Mar Medical Research Institute Barcelona, Barcelona, Spain; [12]Catalan Institute for Research and Advanced Studies, Barcelona, Spain.

*S. Tejedor Vaquero and H. Neuman contributed equally to this paper; **R. Mehr, A. Cerutti, and G. Magri contributed equally to this paper. Correspondence to Andrea Cerutti: acerutti@researchmar.net; Giuliana Magri: gmagri@ub.edu

G. Magri's current affiliation is Immunology Unit, Department of Biomedical Sciences, Faculty of Medicine and Health Sciences, University of Barcelona, Barcelona, Spain. M. Uzzan's current affiliation is Department of gastroenterology, Hospital Henri Mondor, APHP, Creteil France; INSERM U955, IMRB, Creteil, France. E.K. Grasset's current affiliation is Department of Pediatrics, Gale and Ira Drukier Institute for Children's Health, Weill Cornell Medicine, New York, NY, USA.

epithelial cells mediates the translocation of secreted polymeric IgA across epithelial cells (Johansen et al., 2001). During this process, polymeric IgA acquires a pIgR-derived polypeptide called secretory component and thereafter becomes secretory IgA (SIgA), which recognizes intraluminal commensal bacteria (Chen et al., 2020; Brandtzaeg et al., 1999).

In the intestinal lumen, SIgA coats, retains, and functionally modulates commensal bacteria and fungi (Chen et al., 2020; Sterlin et al., 2019, 2020; Rollenske et al., 2021; Pabst and Slack, 2020; Macpherson et al., 2018; Nakajima et al., 2018; Doron et al., 2021). Conversely, gut commensals enhance SIgA production, thereby establishing a microbiota (MB)–SIgA mutualism that enhances gut homeostasis (Fagarasan et al., 2010). Of note, secretory IgA1 (SIgA1) and SIgA2 have been recently found to dually target most gut commensals except colonic Bacteroidetes, which are preferentially recognized by SIgA2 (Sterlin et al., 2020). Despite these advances, the specific biology of IgA1 and IgA2 remains unclear. This gap in knowledge largely stems from the lack of IgA subclasses in mice (Chen et al., 2020).

In adults, most gut IgA is thought to emerge from germinal center (GC) B cells undergoing IgM-to-IgA class switch recombination (CSR) and somatic hypermutation (SHM) through a T cell–dependent (TD) pathway involving CD40 ligand (CD40L) from T follicular helper cells (Seikrit and Pabst, 2021; Chen et al., 2020). In humans, some IgA2 may also derive from a T cell–independent (TI) pathway inducing IgA1-to-IgA2 CSR in memory IgA1$^+$ B cells via a CD40L-like myeloid and epithelial cytokine termed a proliferation-inducing ligand (APRIL) (He et al., 2007). While the question of how frequently sequential IgA1-to-IgA2 class switching occurs in intestinal B cells is still debated (Seikrit and Pabst, 2021; Lin et al., 2014; Fenton et al., 2020); circulating or tonsillar IgA1$^+$ and IgA2$^+$ B cells have been shown to display a significant degree of clonal relatedness (Phad et al., 2022; King et al., 2021; Ellebrecht et al., 2018; Horns et al., 2016; Kitaura et al., 2017). This clonal overlap echoes the largely overlapping transcriptional regulation of the TGF-β–responsive promoters located upstream of Cα1 and Cα2 genes (Islam et al., 1991; Nilsson et al., 1995).

Disruption of gut homeostasis by inflammatory bowel disease (IBD) increases SIgA as well as IgG responses to unique members of the commensal MB (Shapiro et al., 2021; Doron et al., 2021), including colitogenic bacteria (Palm et al., 2014). These findings correlate with the expansion of intestinal B cells and PCs, including poorly diversified IgG-secreting plasmablasts (PBs) (Uzzan et al., 2022). Yet, the biology of PCs expressing IgA1 or IgA2 and the specific reactivity of SIgA1 and SIgA2 to the gut MB from IBD patients remain elusive.

Here, we combined high-throughput and standard approaches to gain new insights into human gut IgA subclasses. We found that IgA1$^+$ and IgA2$^+$ clones from the non-inflamed gut mucosa were largely clonally related and comparably hypermutated, with a fraction of them expressing identical variable (V) region sequences. Moreover, under homeostasis, SIgA1 and SIgA2 antibodies dually targeted beneficial commensals, including *Akkermansia muciniphila*. Disruption of homeostasis by IBD augmented the binding of SIgA1 to pathobionts, including *Escherichia coli* (*E. coli*) as well as members of the Erysipelotrichaceae family. This change was associated with the expansion of short-lived IgA1$^+$ plasmablasts combined with the depletion of long-lived IgA2$^+$ PCs. Concomitantly, IBD decreased dually coated beneficial commensals, including *A. muciniphila*. Thus, while gut homeostasis fosters prominent IgA2 responses, which may promote the retention of beneficial commensals, IBD favors dominant IgA1 responses, which may perpetuate gut dysbiosis and inflammation.

Results

IgA2$^+$ PCs emerge along with IgA1$^+$ PCs early after birth and in adults exceed IgA1$^+$ PCs in the distal gut

The human intestinal IgA repertoire follows a maturation program that co-develops with the assembly of the gut MB during the first 2 years of life (Planer et al., 2016). We first analyzed human gut tissues by immunofluorescence analysis (IFA) to determine age-related changes in the frequency of IgA1$^+$ and IgA2$^+$ cells. IgA$^+$ cells were absent in fetal samples, before gut colonization by the MB, and remained undetectable up to 2 wk after birth (Fig. 1, A and B). Gut IgA1$^+$ PCs started to appear along with gut IgA2$^+$ PCs as early as 6 wk after birth and progressively increased over the first 5 years of life (Fig. 1, A and B). In adults, IgA2$^+$ PCs exceeded IgA1$^+$ PCs in the large bowel, whereas IgA1$^+$ PCs and IgA2$^+$ PCs were equally represented in the distal ileum (Fig. 1, C and D).

Next, we compared the phenotype of gut IgA1$^+$ and IgA2$^+$ PCs by flow cytometry. Compared to naïve B cells, both IgA1$^+$ and IgA2$^+$ PCs expressed more BLIMP-1, CD27, CD43, and CD319, also termed SLAMF7, but less CD20 and CXCR4 (Fig. S1 A). These phenotypic changes are specific to human gut PCs (Magri et al., 2017) and were largely comparable in IgA1$^+$ and IgA2$^+$ subsets. In agreement with the preferential enrichment of IgA2$^+$ PCs in the colon, IgA2$^+$ PCs expressed less CCR9, a CCL25 receptor that guides lymphocytes to the small intestinal mucosa (Mora and von Andrian, 2008), but more G protein-coupled receptor 15 (GPR15), which directs lymphocytes to the colonic mucosa (Kim et al., 2013), compared with IgA1$^+$ PCs (Fig. 1 E). Similarly, a larger fraction of circulating IgA2$^+$ PCs and memory B cells co-expressed the gut homing receptors β7 and GPR15 compared with circulating naïve B cells or non-IgA2$^+$ memory B cells and PCs (Fig. 1, F–H and Fig. S1 B). Thus, IgA2$^+$ PCs emerge with IgA1$^+$ PCs following postnatal gut colonization by commensals, exceed IgA1$^+$ PCs in the colonic mucosa, and include a circulating counterpart expressing the β7 and GPR15 gut-homing receptors.

Intestinal PCs with terminally differentiated phenotype are enriched in IgA2 expression

As shown previously (Landsverk et al., 2017) the human duodenal–jejunal mucosa includes three phenotypically distinct PC subsets characterized by different longevity profiles: early short-lived CD19$^+$CD45$^+$ PCs, also known as CD19$^+$, late long-lived CD19$^-$CD45$^+$ PCs, also termed CD19$^-$, and terminal long-lived CD19$^-$CD45$^-$ PCs, also called CD45$^-$. We followed this phenotypic-functional designation to further characterize IgA$^+$ PCs in the terminal ileum and ascending colon from adult subjects by flow cytometry. We found a comparable frequency of

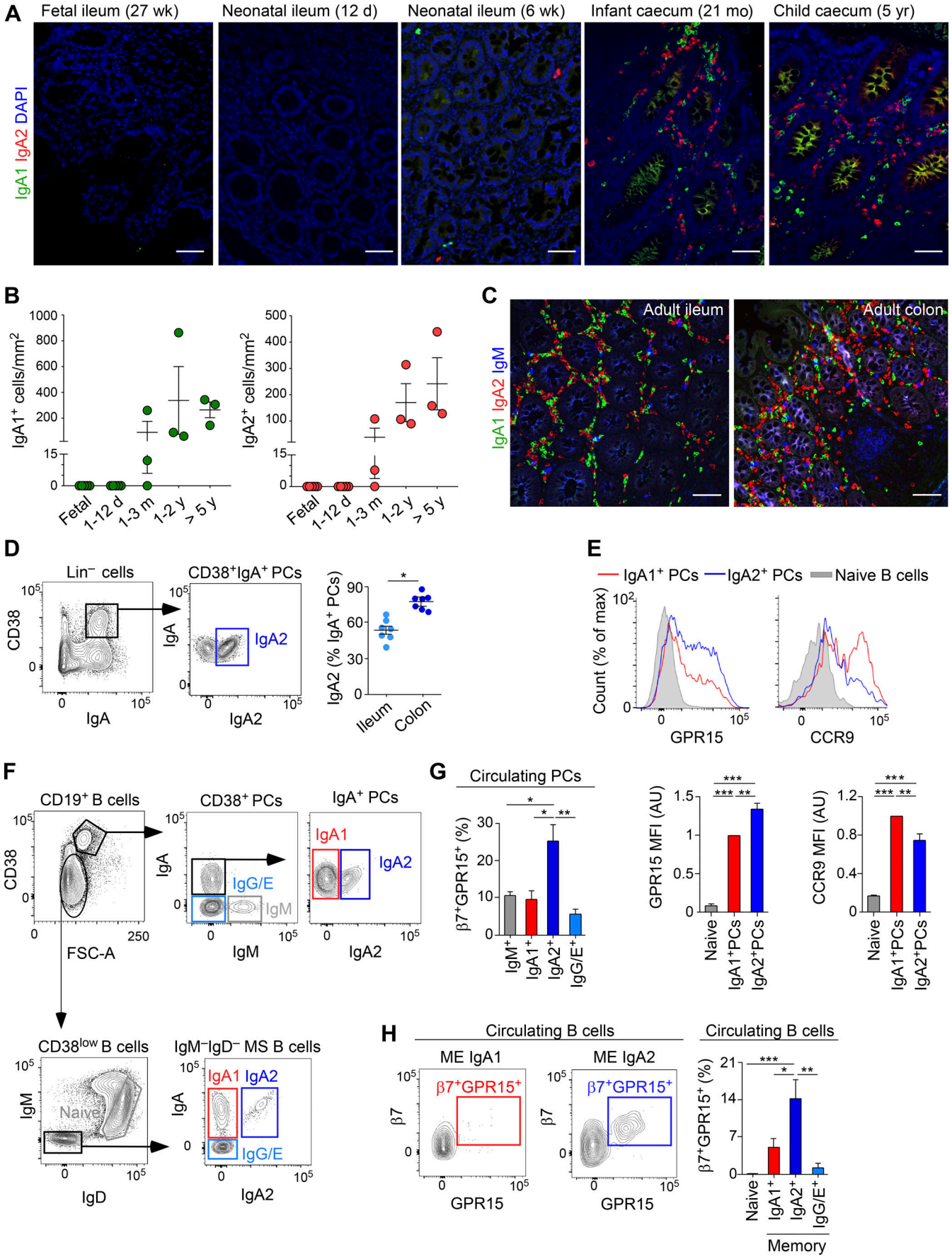
A
Fetal ileum (27 wk)
Neonatal ileum (12 d)
Neonatal ileum (6 wk)
Infant caecum (21 mo)
Child caecum (5 yr)
IgA1 IgA2 DAPI
B
IgA1+ cells/mm2
IgA2+ cells/mm2
Fetal
1-12 d
1-3 m
1-2 y
> 5 y
C
Adult ileum
Adult colon
IgA1 IgA2 IgM
D
Lin− cells
CD38+IgA+ PCs
CD38
IgA
IgA2
IgA2 (% IgA+ PCs)
Ileum
Colon
E
IgA1+ PCs
IgA2+ PCs
Naive B cells
Count (% of max)
GPR15
CCR9
F
CD19+ B cells
CD38+ PCs
IgA+ PCs
IgG/E
IgM
FSC-A
CD38low B cells
IgM−IgD− MS B cells
Naive
IgD
G
Circulating PCs
β7+GPR15+ (%)
IgM+
IgA1+
IgA2+
IgG/E+
GPR15 MFI (AU)
CCR9 MFI (AU)
Naive
IgA1+PCs
IgA2+PCs
H
Circulating B cells
ME IgA1
ME IgA2
β7+GPR15+
β7
GPR15
Memory

Figure 1. **Human intestinal IgA2 emerges along with IgA1 early in life and in adults predominates in distal gut segments. (A)** IFA of IgA1 (green), IgA2 (red), and nuclear DNA (blue) in prenatal (fetal) or postnatal (neonatal, infant, and child) human gut tissues. Original magnification, 20×; scale bar, 50 µm. **(B)** Numbers of IgA1$^+$ and IgA2$^+$ cells per mm^2 in gut tissue from fetal (20–36 wk; *n* = 5), neonatal (1–12 days [d]; *n* = 5), infant (35–64 days; *n* = 3), and child (1–2 years [y], *n* = 3; 5–10 years; *n* = 3) samples. Each dot represents the mean of 1–5 fields/sample. m, months. **(C)** IFA of IgA1 (green), IgA2 (red), and IgM (blue) in the ileum (left) and colon (right) tissues from an adult individual. Original magnification, 20×; scale bar, 50 µm. **(D)** FCA of cell surface CD38, IgA, and IgA2 (left and middle graphs) and frequency of IgA2$^+$ (right graph) cells from the total IgA$^+$ PC pool of viable DAPI$^-$Lin$^-$CD38^{hi}CD10$^-$IgA$^+$ cells from the terminal ileum or ascending colon of adult individuals. **(E)** FCA (upper histograms) and mean fluorescence intensity (MFI, lower bar plots) of cell surface GPR15 and CCR9 on naive B cells, IgA1$^+$ PCs, and IgA2$^+$ PCs from the human terminal ileum. MFI is shown as arbitrary units (AUs) calculated in comparison to the ones of IgA1$^+$ PCs, which were set as 1. **(F)** FCA of CD38, IgA, IgM, IgD, and IgA2 on CD19$^+$ B cells from human peripheral blood. **(G and H)** Frequencies of β7$^+$GPR15$^+$ cells within IgM$^+$, IgA1$^+$, IgA2$^+$, or IgG/E$^+$ PC subsets (G) as well as naive or class-switched memory IgA1$^+$, IgA2$^+$, and IgG/E$^+$ B cell subsets (H) from human peripheral blood as defined in F. Data show one of at least three experiments yielding similar results (A, C, and F) or summarize results from three to five (B), seven (D), three (E, lower left graph and G) or five (E, lower right graph and H) donors. Results are presented as mean ± SEM; Wilcoxon matched paired test (D) and one-way ANOVA with Tukey's post-hoc test (E, G, and H). *P < 0.05, **P < 0.01, ***P < 0.001. See also Fig. S1.

CD19$^+$, CD19$^-$, and CD45$^-$ subsets in the IgA$^+$ PC pool from both terminal ileum and ascending colon (Fig. 2 A). Compared with naïve B cells, CD19$^+$IgA$^+$, CD19$^-$IgA$^+$, and CD45$^-$IgA$^+$ PCs expressed more BLIMP-1, CD27, and CD319 but less CD20 and HLA-DR (Fig. S1 C), all of which are hallmarks of mature PCs.

When compared with the early CD19$^+$IgA$^+$ PC subset, the late CD19$^-$IgA$^+$ PC subset and terminal long-lived CD45$^-$IgA$^+$ PC subset expressed more CD138 (Fig. 2 B), which is a hallmark of terminally differentiated PCs. In addition, a larger fraction of late CD19$^-$IgA$^+$ PCs and terminal CD45$^-$IgA$^+$ PCs expressed CD56 (Fig. 2 B), an adhesion molecule potentially involved in PC tissue retention (Mei et al., 2015). In contrast, early CD19$^+$IgA$^+$ PCs expressed more CD71 and CD43 (Fig. 2 C), which are proliferation and activation molecules, respectively, expressed by actively cycling B cells (Ellebedy et al., 2016; Inui et al., 2015). Accordingly, IFA and flow cytometry showed that the gut lamina propria (LP) included a small population of IgA$^+$CD138$^-$Ki-67$^+$ PBs (Fig. 2 D), which mostly belonged to the CD19$^+$ PC subset (Fig. 2, E and F).

Next, we dissected IgA2 expression in distinct PC and B cell subsets. We found more IgA2$^+$ cells in late CD19$^-$IgA$^+$ and terminal CD45$^-$IgA$^+$ PCs compared with early CD19$^+$IgA$^+$ PCs from the ascending colon (Fig. 2 G). In the terminal ileum, IgA2$^+$ cells accounted for about 30% of IgA$^+$ GC B cells, 50% of IgA$^+$ memory B cells, 60% of early CD19$^+$IgA$^+$ PCs, 70% of late CD19$^-$IgA$^+$ PCs, and >80% of terminal CD45$^-$IgA$^+$ PCs (Fig. 2 H). Thus, IgA1 and IgA2 expression differs in distinct gut PC subsets, with IgA2 being enriched compared with IgA1 in late CD19$^-$IgA$^+$ and terminal CD45$^-$IgA$^+$ PC subsets.

Intestinal IgA1$^+$ and IgA2$^+$ cells are somatically mutated and largely clonally related

To gain new insights into the ontogeny of IgA1$^+$ and IgA2$^+$ PCs and the clonal architecture of intestinal B cells in homeostasis, we performed high-throughput Ig repertoire analysis of naïve B cells, unswitched and switched memory B cells, and PCs sorted from the terminal ileum or ascending colon of four adult individuals (Table S5). IgA1 and IgA2 transcripts were amplified from memory and plasma cell pools through the use of an antisense pan-IgA primer and IgA subclass resolution was achieved by computational analysis of Ig heavy chain variable (IGHV) gene sequences. In total, 10,182,511 IGHV gene sequences from four donors were obtained through high-throughput sequencing (HTS). To minimize the inclusion of PCR and sequencing errors, cDNA molecules were labeled with unique molecular identifier (UMI) barcodes during library preparation.

We first analyzed the repertoire diversity of experienced B cells per donor and found comparable diversity profiles (Fig. S2 A). Pearson's correlation coefficient analysis of IGHV gene segment usage indicated that memory IgA1$^+$ and IgA2$^+$ B cells as well as IgA1$^+$ and IgA2$^+$ PCs segregated away from naive, memory IgM$^+$ B cells, and IgM$^+$ PCs, but hierarchically clustered together (Fig. 3 A). Unlike naive IgM$^+$ B cells, IgA1$^+$ and IgA2$^+$ memory B cells and PCs expressed mutated IGHV sequences (Fig. 3 B). Mutation frequencies and the percentages of unmutated IGHV genes were similar in IgA1$^+$ and IgA2$^+$ memory B cells or PCs, independent of their tissue or cell origin (Fig. 3 B).

To explore clonal relationships, we searched for clones unique to each subclass or shared by different subclasses. IgA1$^+$ and IgA2$^+$ cells shared more clones compared with IgA1$^+$ and IgM$^+$ cells or IgA2$^+$ and IgM$^+$ cells (Fig. 3 C). We then visualized and quantified the ontogenetic affiliations of IgA2$^+$ PCs with other memory B cells and PC subsets from the same or different gut segments by means of Circos plots and bar plots after clonal grouping (Fig. 3, D–F). Aside from their expected clonal relatedness to IgA2$^+$ memory B cells, IgA2$^+$ PCs showed the highest degree of connectivity with IgA1$^+$ PCs and IgA1$^+$ memory B cells and, to a lesser extent, antigen-experienced IgM$^+$ B cells (Fig. 3 D). Besides being clonally related to ileal IgA1$^+$ PCs, ileal IgA2$^+$ PCs showed also some clonal relatedness with colonic PCs (Fig. 3 E). The analysis of the isotype and population composition of clones containing IgA2 sequences from ileal PCs indicated that >50% of them also contained IgA1 sequences, including a large proportion of clones comprising sequences from memory and PCs from identical or more distal gut tissues (Fig. 3 F).

The clonal relationship between IgA1$^+$ and IgA2$^+$ cells was further confirmed in one additional histologically normal ileal tissue sample by single cell V(D)J RNA sequencing, as visualized by the honeycomb plot (Fig. 3 G) and a representative lineage tree (Fig. 3 H). Thus, gut IgA1$^+$ and IgA2$^+$ memory B cells and PCs express a post-GC mutational profile and are extensively clonally related in homeostasis.

Some intestinal IgA2$^+$ cells may emerge from IgA1$^+$ precursors without accumulating supplemental SHM

To further clarify the ontogenetic link between IgA2$^+$ and IgA1$^+$ cells from the terminal ileum or ascending colon, we

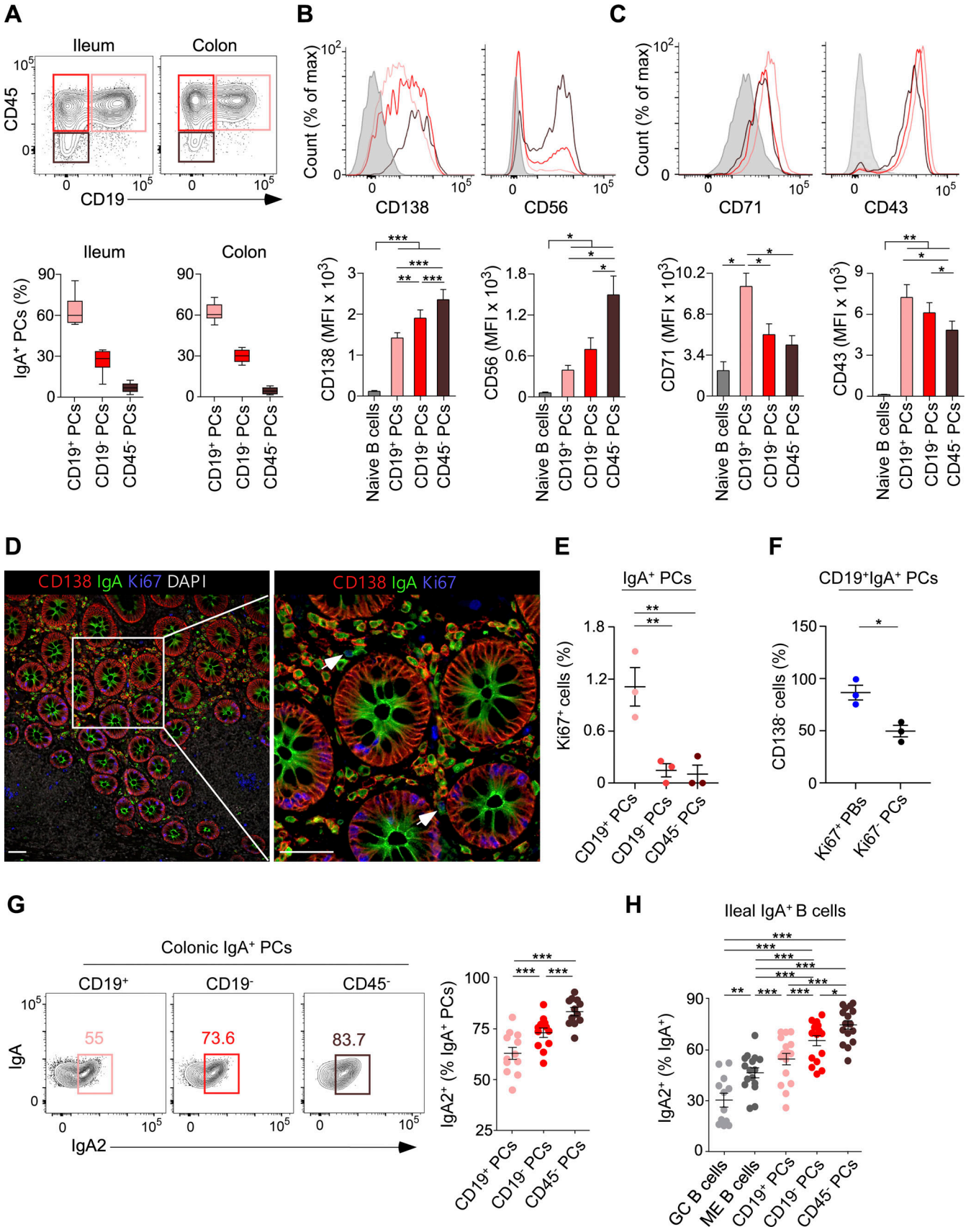

Figure 2. **Human intestinal long-lived CD19⁻ PCs are enriched in IgA2 expression. (A)** FCA of CD45 and CD19 on total CD10⁻CD38^{hi}IgA⁺ PCs from the terminal ileum or ascending colon of a representative adult individual (upper panel) or summaries of the frequencies of ileal or colonic CD19⁺CD45⁺ (or CD19⁺),

$CD19^-CD45^+$ (or $CD19^-$), and $CD19^-CD45^-$ (or $CD45^-$) PC subsets (bottom panel) within total IgA^+ PCs from adult donors under study. **(B and C)** FCA of CD138 and CD56 (B) or CD71 and CD43 (C) on control naive B cells (gray) as well as $CD19^+$ (pink), $CD19^-$ (red), and $CD45^-$ (brown) PC subsets from total ileal or colonic $Lin^-CD10^-CD38^{hi}IgA^+$ PCs of adult individuals. Upper panels: overlaid histogram profiles of CD138, CD56, CD71, or CD43 on PC subsets from a representative donor; lower panels: summaries of MFI values of CD138, CD56, CD71, and CD43 on PC subsets. **(D)** IFA of IgA (green), CD138 (red), Ki-67 (blue), and DAPI (white) in human colonic LP. Arrows point to actively proliferating $IgA^+Ki\text{-}67^+CD138^-$ PBs. Original magnification, 20× (left) and 60× (right); scale bar, 50 µm. **(E)** FCA of the frequency of $Ki67^+$ cells within IgA class-switched ($CD10^-$ $CD38^+$ IgA^+) $CD19^+$, $CD19^-$, and $CD45^-$ PC subsets from the human intestine. **(F)** FCA of the frequency of $CD138^-$ cells within $CD19^+IgA^+Ki67^+$ PBs or $CD19^+IgA^+$ $Ki67^-$ PCs. **(G)** FCA of IgA and IgA2 expression and frequency of $IgA2^+$ cells within each IgA class-switched $CD19^+$, $CD19^-$, and $CD45^-$ PC subsets from human ascending colon. Numbers in flow plots show % of $IgA2^+$ cells within each subset. **(H)** Frequencies of $IgA2^+$ cells within $CD19^+CD10^+CD27^+CD38^{int}IgA^+$ GC B cells, $CD19^+CD10^-CD38^+IgA^+$ memory (ME) B cells, and IgA class-switched $CD19^+$, $CD19^-$, and $CD45^-$ PC subsets from the human terminal ileum. Data show one of at least three experiments yielding similar results (D) or summarize results from 10 (A, left panel), 8 (A, right panel) 20 (B, left panel) 5 (B, right panel; C), 3 (E and F), 12 (G), or 16 (H) donors. Results are presented as mean ± SEM; One-way ANOVA with Tukey's post-hoc test (B, C, E, G, and H) and paired Student's *t* test (F). *P < 0.05, **P < 0.01, ***P < 0.001. See also Fig. S1.

reconstructed their phylogenetic relationships by combining Ig gene repertoire with lineage tree analysis. The resulting lineage trees were further examined through the in-house PopTree program (Neuman et al., 2022). As typically seen in normal Ig repertoires, lineage trees varied greatly in size (i.e., number of nodes), degree of branching (i.e., number of leaves, root outgoing degree), and branch lengths (i.e., minimum path length) over two to four orders of magnitude (Fig. S2 B). Additionally, as expected, a substantial proportion of lineage trees contained sequences of mixed isotypes (Fig. S2, C and D).

First, we quantified transitions from one antibody class or subclass to another, which could reflect CSR. Intestinal IgM^+ cells comparably transitioned to $IgA2^+$ or $IgA1^+$ cells, whereas $IgA1^+$ cells transitioned to $IgA2^+$ cells more than IgM^+ cells did (Fig. 4, A and B). Of note, in addition to CSR, lineage tree reconstruction permits to quantify SHM (Barak et al., 2008) more accurately than other methods (Neuman et al., 2022). While CSR can occur inside or outside mucosal GCs (Bunker et al., 2015; He et al., 2007; Reboldi et al., 2016; Roco et al., 2019; Wang et al., 2017), SHM mostly occurs in mucosal GCs in response to TD signals (Chen et al., 2020; Kawamoto et al., 2012, 2014; Nowosad et al., 2020; Seikrit and Pabst, 2021). Moreover, SHM can occur in pre-existing memory IgM^+ or IgA^+ B cells re-entering mucosal GCs in adults with a stable MB (Lindner et al., 2015; Magri et al., 2017).

Consistent with this possibility, we could detect some transitions from $IgA1^+$ GC B cells into $IgA2^+$ GC and memory B cells (Fig. 4 C) as well as transitions from $IgA1^+$ ME B cells to $IgA2^+$ PCs, with or without the accumulation of new mutations (Fig. 4 D and Fig. S3 A), which presumably took place inside or outside mucosal GCs, respectively. The GC origin of some sequential IgA1-to-IgA2 switching events was further visualized by Circos plot analysis (Fig. S3 B). As expected, $IgA1^+$ GC B cells were found clonally linked to $IgA2^+$ GC, as well as $IgA1^+$ PCs or $IgA2^+$ PCs (Fig. S3 B, left). Remarkably, IgM^+ GC B cells were largely clonally linked to IgM^+ PCs (Fig. S3 B, right), which suggests a less prominent direct IgM-to-IgA switching in intestinal GCs.

Lineage tree analysis further allows the enumeration of mutation frequencies on a per-tree basis (Neuman et al., 2022). In (sub)class-specific clones, $IgA1^+$ and $IgA2^+$ cells had comparable average numbers of mutations, which were higher than the average numbers of mutations observed in IgM^+ B cells (Fig. 4 E). In clones shared by IgA1, IgA2, and/or IgM, the average number of mutations was not significantly different from that found in IgA1-only clones (Fig. S3 C). In contrast, the average mutation numbers in clones shared by all three isotypes, i.e., $IgA2^+$, $IgA1^+$, and IgM^+ clones, were significantly larger than the average mutation number in IgA2-only clones (Fig. 4 F).

Next, we quantified the proportions of transitions with ≤2 mutations, presumably GC-independent, and transitions with >2 mutations, likely GC-dependent (Berkowska et al., 2011). Transitions from IgM to IgA1 or from IgM to IgA2 as well as transitions from IgA1 to IgA2 mostly occurred independently of SHM (Fig. 4 G). Moreover, transitions from IgA1 to IgA2 were less frequently associated with >2 mutations compared to transitions from IgM to IgA1 or from IgM to IgA2 (Fig. 4 G). Of note, memory B cell-to-memory B cell transitions from IgA1 to IgA2 were more frequently associated with >2 mutations compared to memory B cell-to-PC transitions from IgA1 to IgA2 (Fig. 4 H). This difference was not observed in transitions from IgM to IgA1 or from IgM to IgA2 (Fig. S3 D).

Lastly, we evaluated IgA2 induction by human splenic non-switched B cells or human intestinal $IgA1^+$ B cells following exposure in vitro to TD (i.e., CD40L, IL-21) or TI (i.e., CpG-DNA) signals supplemented with IgA-inducing signals (TGF-β, IL-10, B cell activating factor [BAFF], APRIL) (Cerutti, 2008; Magri et al., 2017). Splenic non-switched B cells differentiated more extensively into PCs in response to TD stimuli, but TI stimuli induced more $IgA2^+$ PCs compared to TD stimuli (Fig. 4 I). Finally, intestinal $IgA1^+$ B cells exposed to TD or TI stimuli comparably differentiated into $IgA2^+$ PCs (Fig. 4 J). Thus, while some gut $IgA2^+$ B cells originate from $IgA1^+$ B cells through a GC reaction involving the induction of additional SHM compared with the starting SHM observed in precursor $IgA1^+$ clones, some other $IgA2^+$ ME B cells and PCs seem to originate from $IgA1^+$ precursor clones without accumulating supplemental SHM.

Intestinal SIgA1 and SIgA2 show shared as well as unique reactivity to mucus-embedded bacteria

Next, we wondered whether SIgA1 and SIgA2 dually targeted the gut MB. Thus, we devised a flow cytometric strategy that quantifies microbial coating by both SIgA2 and SIgA1 with subclass-specific fluorochrome-conjugated antibodies. First, we determined SIgA and SIgM binding to the fecal MB from healthy controls (HCs) and control patients with selective IgA deficiency (SIgAD). As reported previously (Fadlallah et al., 2018), SIgAD patients had little or no SIgA-only coated MB but significantly

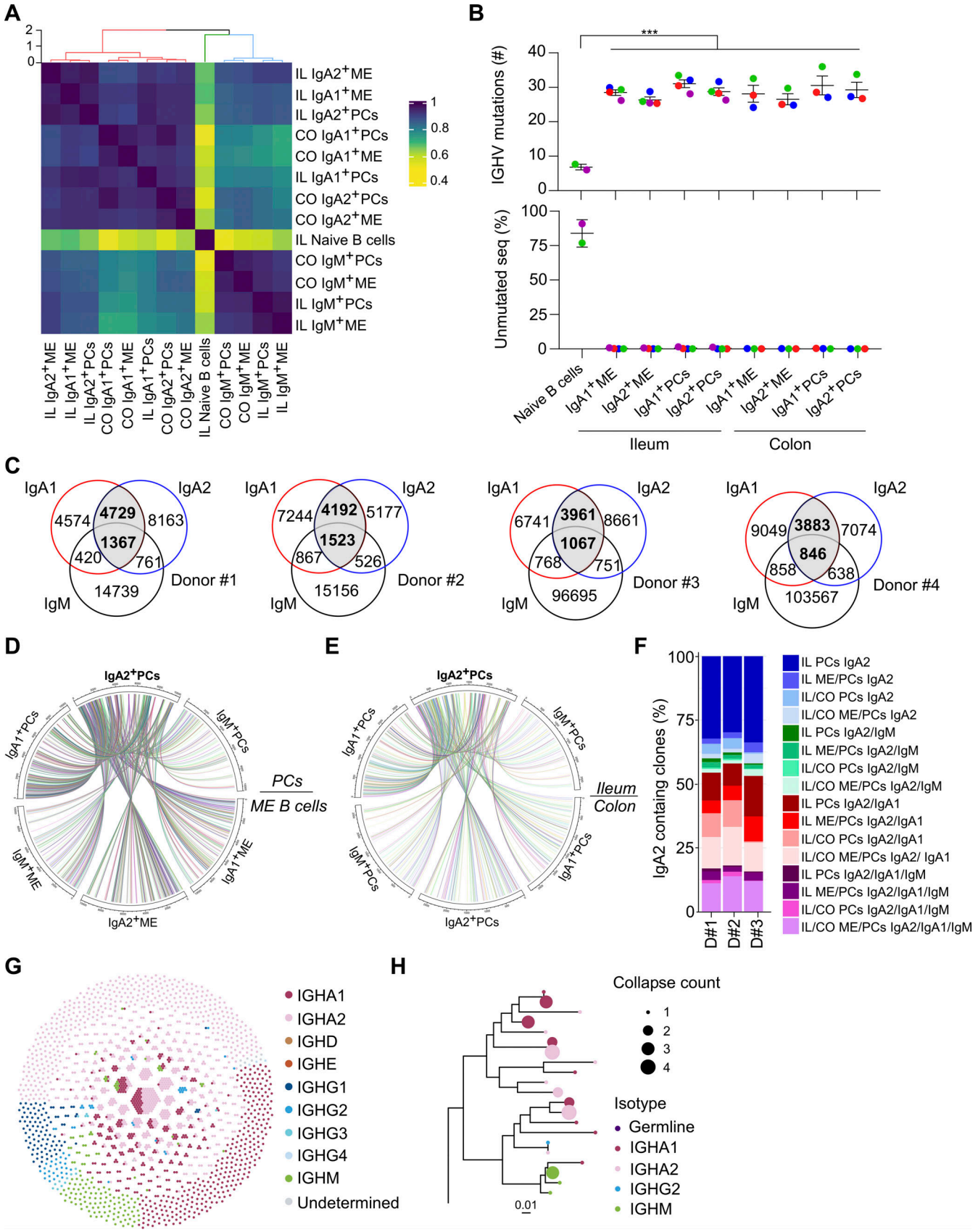

Figure 3. **Human intestinal IgA2⁺ B cells express a post-GC mutational profile and are extensively clonally related to IgA1⁺ B cells. (A)** Pearson's correlation coefficient matrix of IGHV gene segment usage by naïve B cells and paired IgM⁺, IgA1⁺, and IgA2⁺ memory (ME) B cells and PCs from human terminal ileum (IL) and ascending colon (CO) grouped according to their correlation patterns by hierarchical clustering, based on the Ward.D2 method. **(B)** Mean

numbers (#) of IGHV gene mutations per sequence (upper panel) and proportions of unmutated IGHV gene sequences (lower panel) in naïve B cells and IgA1$^+$ or IgA2$^+$ B cell subsets as in A. Each color represents a different donor (D); D#1, blue, D#2 red, D#3 green, and D#4, purple. **(C)** Venn diagrams showing the numbers of IGHV clones unique to each isotype as well as the numbers of IGHV clones shared by two or three isotypes in each donor. **(D and E)** Circos plots from D#3 depicting clonal relationships between PCs and ME B cells (D) or between PCs from different tissues (E) expressing different isotypes. The reference cell subset is shown in bold. **(F)** Bar plots depicting the isotype and population composition of clones containing IgA2 sequences from D#1, D#2, and D#3. **(G)** Honeycomb plot generated from single-cell V(D)J RNA sequencing data obtained from a histologically normal ileal sample. Single cells are represented as dots and each clonotype is represented as a hexagonal cluster of cells. Cells were colored according to their isotype. **(H)** Representative lineage tree from sequencing data as in G built using the maximum likelihood method. Each tree represents a B cell clone, and each dot, a leaf node. The size of each dot reflects the number of B cells (sharing the same sequence) that the node represents. Data show one donor (G and H), one representative result from four biological replicates (D and E), or summarize results from three (F) or four different donors (A–C). Error bars, SEM; and one-way ANOVA with Tukey's post-hoc test (B). ***P < 0.001. See also Fig. S2.

more SIgM-only coated MB compared to HCs (Fig. 5 A). Next, we measured SIgA1 and SIgA2 binding to fecal MB using our flow cytometry strategy. While HCs consistently showed readily detectable fractions of fecal MB coated by SIgA2 alone or both SIgA2 and SIgA1 as well as a very small fraction of MB coated by SIgA1 alone, patients with SIgAD almost completely lacked MB coated by SIgA2 but in some individuals included a few microbes coated by SIgA1 only isotype (Fig. 5 B). These results revealed a unique pattern of MB coating in SIgAD patients and confirmed the accuracy of our subclass-specific microbiome profiling.

Given that SIgA may form a concentration gradient from the mucosal epithelium to the center of the gut lumen and from proximal to distal gut segments (Macpherson et al., 2018; Pabst and Izcue, 2022), SIgA binding to fecal bacteria may not reflect that of commensals positioned next to the gut epithelium. Thus, we also analyzed the SIgA coating profiles of mucus-embedded bacteria from paired human samples of terminal ileum and ascending colon. When mucus-embedded bacteria were analyzed, we found that most IgA-coated bacteria were dually coated by SIgA1 and SIgA2 in both the terminal ileum and ascending colon (Fig. 5 C). Of note, mucus-embedded bacteria coated only by SIgA1 were consistently more frequent in the terminal ileum compared with the ascending colon, whereas mucus-embedded bacteria coated only by SIgA2 were consistently more frequent in the ascending colon (Fig. 5 D).

Then, we sought to analyze the reactivity of free SIgA1 and SIgA2 from the terminal ileum and ascending colon by bacterial flow cytometry using a few representative gut bacterial strains. First, we assessed the relative abundance of free SIgA1 and SIgA2 by enzyme-linked immunosorbent assay (ELISA). MB-free SIgA1 was more abundant in mucus samples from the terminal ileum compared with the ascending colon, whereas MB-free SIgA2 was comparably abundant in the terminal ileum and ascending colon (Fig. 5 E). We then comparatively analyzed the reactivity of bacterial-free SIgA1 and SIgA2 from the terminal ileum and ascending colon to a few representative gut bacterial strains, i.e., *Bacteroides fragilis*, *Ruthenibacterium lactatiformans*, *A. muciniphila*, and *Bifidobacterium longum*. This analysis revealed the presence of interindividual as well as species-specific variability in the binding profiles with consistently less reactivity of SIgA1 and SIgA2 from the terminal ileum compared with the ascending colon (Fig. 5 F). In particular, when the reactivity of free SIgA1 and SIgA2 from the ascending colon was analyzed (Fig. 5, G and H), no consistent binding of either free SIgA1 or free SIgA2 to *B. fragilis* was found in the large majority of samples. In contrast, in most of the samples analyzed, we detected the binding of free SIgA2 but not free SIgA1 to *R. lactatiformans*, a beneficial *Ruminococcaceae* family member associated with gut homeostasis (Magri et al., 2017) (Fig. 5, G and H). Finally, SIgA1 and SIgA2 from the majority of colonic mucus samples analyzed comparably coated *A. muciniphila* and *B. longum* (Fig. 5, G and H), two beneficial commensals often depleted in IBD (Ansaldo et al., 2019; Manichanh et al., 2012; Guarner and Malagelada, 2003). Thus, while most SIgA2 coats mucus-embedded bacteria dually targeted by SIgA1, some SIgA2 shows a unique reactivity to some microbes, including beneficial gut commensals.

Gut inflammation is associated with the expansion of IgA1$^+$ PBs and depletion of IgA2$^+$ PCs

To gain new insights into the biology of IgA1 and IgA2 subclasses, we examined whether gut IgA1 and IgA2 responses showed any alteration in IBD. These gastrointestinal inflammatory disorders encompass Crohn's disease (CD) and ulcerative colitis (UC) and feature dysregulated antibody responses to the intestinal MB (Caruso et al., 2020; De Souza and Fiocchi, 2015; Palm et al., 2014; Shapiro et al., 2021). First, we compared the frequencies of IgA$^+$, IgM$^+$, and IgG$^+$ (defined as IgA$^-$ and IgM$^-$) PCs and memory B cells from gut biopsies obtained from HCs and clinically active IBD patients (Table S1). In agreement with studies published previously (Uzzan et al., 2022; Martin et al., 2019), flow cytometry showed comparable frequencies of IgM$^+$ PCs but lower and higher frequencies of IgA$^+$ and IgG$^+$ PCs, respectively, in IBD patients compared with HCs (Fig. 6, A and B).

We then analyzed the frequencies and absolute numbers of IgA1$^+$ or IgA2$^+$ cells from intestinal PC and memory B cell compartments by flow cytometry and IFA. Compared with HCs, IBD patients showed higher frequencies of IgA1$^+$ PCs but lower frequencies of IgA2$^+$ PCs (Fig. 6 C). Aside from exhibiting lower absolute numbers of gut IgA2$^+$ PCs and increased absolute numbers of IgA1$^+$ PCs, IBD patients exhibited lower frequencies of IgA2$^+$ memory B cells in both intestine and circulation (Fig. 6, D and E; and Fig. S4 A).

This shift from dominant gut IgA2 responses in HCs to dominant gut IgA1 responses in IBD patients was associated with massively higher frequencies of early short-lived CD19$^+$IgA$^+$ PCs and a proportional depletion of long-lived late and terminal CD19$^-$IgA$^+$ and CD45$^-$IgA$^+$ PCs, respectively (Fig. 6 F and Fig. S4 B). Such a remodeling of the mucosal PC repertoire occurred only in inflamed gut segments from clinically active IBD patients, whereas non-inflamed gut segments remained mostly

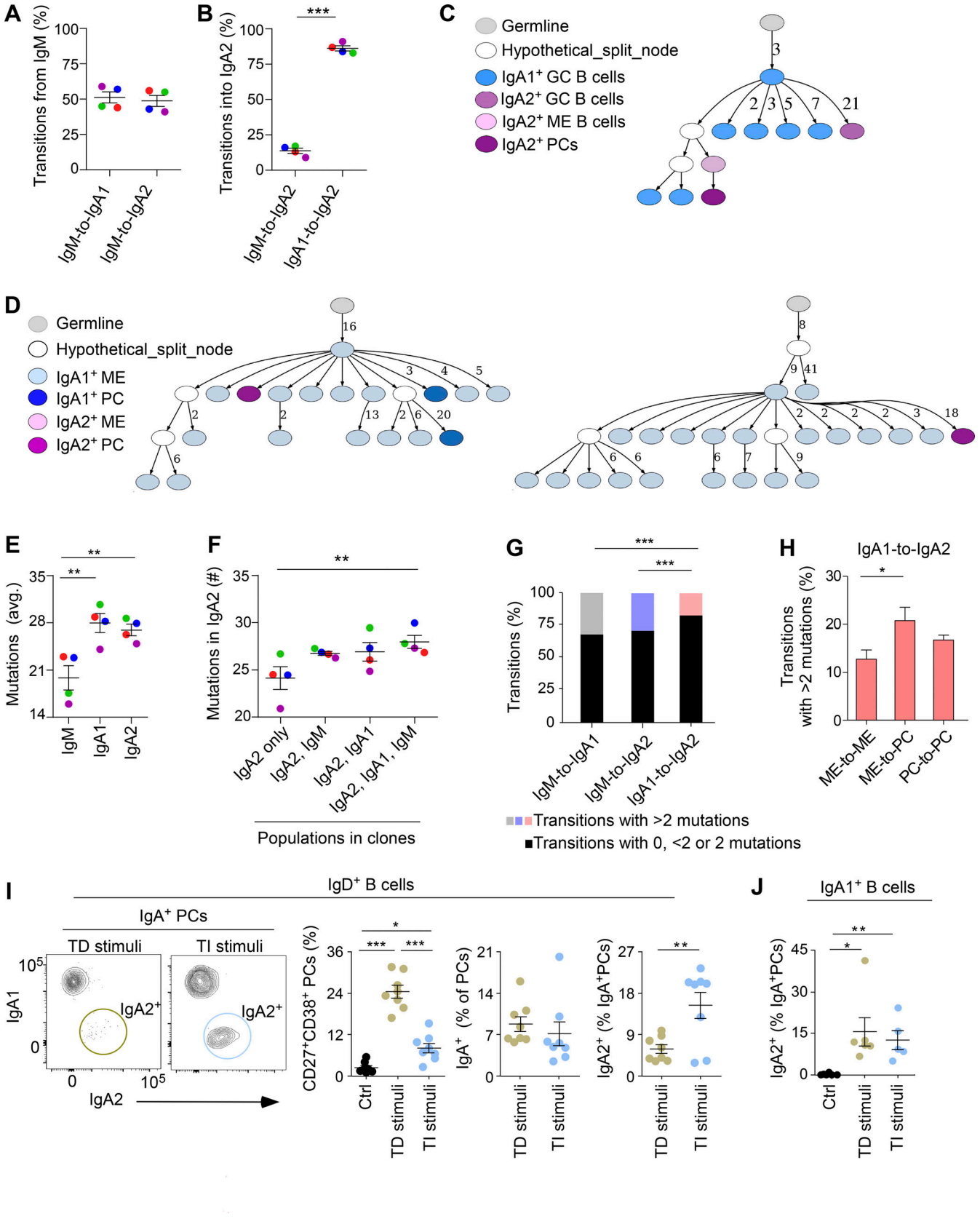

Figure 4. **A fraction of human intestinal IgA2⁺ B cells may originate from mutated IgA1⁺ clones via sequential IgA1-to-IgA2 CSR uncoupled from SHM. (A and B)** Frequencies of transitions into IgA1 or IgA2 out of all transitions from IgM to IgA (A) and from IgM or IgA1 out of all transitions into IgA2 (B) quantified by lineage tree analysis. Donor (D)#1, blue; D#2, red; D#3, green; D#4, purple. **(C and D)** Lineage trees from two distinct donors. Color codes are shown above or below each tree. Trees were colored using a custom script and drawn with a local version of Graphviz. Numbers indicate mutations; edges with no attached

number indicate one mutation. ME, memory. **(E)** Average numbers of IGVH mutations per clone in IgM$^+$, IgA1$^+$, and IgA2$^+$ clones (excluding clones with more than one Ig class or subclass), counted on lineage trees along each path from the root (germline sequence) to each leaf sequence, then averaged for each tree, and again for each donor. D#1, blue; D#2, red; D#3, green; D#4, purple. **(F)** Average numbers of mutations in IgA2 sequences belonging to clones sharing other Ig classes and/or subclasses, counted as in E. D#1, blue; D#2, red; D#3, green; D#4, purple. **(G)** Relative proportions of transitions with up to two mutations and transition with >2 mutations. The numbers of mutations were calculated by measuring the number of edges separating distinct isotypes in each lineage tree. **(H)** Frequencies of IgA1 to IgA2 transitions with >2 mutations within or between different cell populations. **(I)** FCA of IgA1 and IgA2 on in vitro induced IgA$^+$ PCs and frequencies of in vitro induced total CD27$^+$CD38$^+$ PCs, IgA$^+$ cells (shown as % of total PCs), and IgA2$^+$ PCs (shown as % of IgA$^+$ PCs) after culturing splenic IgD$^+$ B cells with TD (CD40L + IL-21) or TI (CpG-DNA) stimuli supplemented with IgA-inducing signals (TGF-β, IL-10, BAFF, APRIL) for 6 days. Ctrl (control), medium alone. **(J)** Frequency of in vitro induced IgA2$^+$ PCs (shown as % of IgA$^+$ PCs) gated as in J after culturing ileal IgA1$^+$ B cells with TD (CD40L + IL-21) or TI (CpG-DNA) stimuli supplemented with IgA-inducing signals (TGF-β, IL-10, BAFF, and APRIL) for 6 days. Ctrl (control), medium alone. Data show two representative results out of four biological replicates (C and D) or summarize results from four different donors (A, B, and E–H) or from eight (I) or five (J) independent experiments. Error bars, SEM; two-tailed paired Student's *t* test (A and B), one-way ANOVA with Tukey's post-hoc test (E–H and I, left panel), two-tailed Mann–Whitney *U* test (I, middle and right panels) and Kruskal–Wallis test (J). *P < 0.05, **P < 0.01, ***P < 0.001. See also Fig. S3.

unaffected (Fig. 6 G and Fig. S4 C). Consistent with the extensive increase of intestinal early short-lived CD19$^+$IgA$^+$ PCs, IFA revealed an expansion of IgA1$^+$Ki-67$^+$ PBs in the gut LP from patients with IBD (Fig. 6, H–J).

This finding was associated with the presence of a larger circulating fraction of CD71$^+$IgD^{low} B cells in IBD patients (Fig. S4 D). These B cells, which correspond to recently antigen-activated B cells (Ellebedy et al., 2016), mostly belonged to memory IgA1$^+$ B cells (Fig. S4 E). Thus, disruption of gut homeostasis by IBD shifts distal intestinal IgA responses from an IgA2-dominated PC profile to an IgA1-dominated PC profile that stems from the depletion of long-lived IgA2$^+$ PCs combined with the expansion of short-lived IgA1$^+$ PBs.

Inflammation alters both coating and selection of gut mucus-embedded bacteria by SIgA1 and SIgA2

Given that SIgA may shape the composition of the human gut MB (Fadlallah et al., 2018; Kubinak and Round, 2016), we elucidated the relative impact of SIgA1 and SIgA2 binding to intestinal microbes by profiling fecal bacteria from six HCs through a combination of IgA1- and/or IgA2-based bacterial sorting and 16S ribosomal RNA (16S rRNA) sequencing (Fig. 7 A). In a given donor sample, the composition of enriched fractions of fecal bacteria coated by SIgA1 alone (SIgA1$^+$SIgA2$^-$), both SIgA1 and SIgA2 (SIgA1$^+$SIgA2$^+$), SIgA2 alone (SIgA1$^-$SIgA2$^+$), or uncoated (SIgA1$^-$SIgA2$^-$) varied at both phylum and genus levels (Fig. 7 B).

We then applied a log-based enrichment index (EI), to identify bacterial species enriched in each of the above bacteria fractions. Aside from an enrichment of the beneficial Verrucomicrobia *A. muciniphila* in SIgA1$^+$SIgA2$^+$ fraction, an enrichment of potentially pathogenic Gammaproteobacteria was detected together with a depletion of Clostridia in single-coated SIgA1$^+$SIgA2$^-$ enriched bacterial subset (Fig. 7, C–E).

Next, we quantified the binding of SIgA1 and SIgA2 to fecal commensals in HCs and patients with UC or acute enteritis (Table S2). As reported by an earlier study (Palm et al., 2014), bacteria coated by SIgA were increased in UC patients compared with HCs (Fig. 7 F). This increase was mostly due to the higher frequency of dually coated SIgA1$^+$SIgA2$^+$ gut microbes (Fig. 7 F), which were also increased in patients with acute enteritis (Fig. 7 G).

Considering that heightened IgA1 production likely drives the expansion of SIgA1$^+$SIgA2$^+$ gut microbes in UC, we subsequently compared the composition of fecal bacteria from HCs and UC patients by combining SIgA1-based bacteria sorting with 16S rRNA gene sequencing (Fig. 7 H). At the beginning of this experimental approach, we sorted total viable fecal bacteria (input) to analyze their global composition. As reported previously (Pascal et al., 2017), total fecal bacteria from both HCs and UC patients showed comparable global community profiles as well as Faith's phylogenetic richness and Shannon index (Fig. S5, A–C), which measure α diversity.

Along the same lines, principal component analysis (PCA) performed on measurements of Bray Curtis β diversity failed to clearly segregate fecal bacteria in UC patients and HCs (Fig. S5 D). Yet, in agreement with a study published previously (Shapiro et al., 2021), the Verrucomicrobia member *A. muciniphila* was depleted in UC patients compared with HCs (Fig. 7 I). We subsequently applied a log-based EI to identify bacterial species enriched in SIgA1$^+$ fractions compared with input and found an enrichment of Verrucomicrobia in the SIgA1$^+$-coated fraction, whereas Bacteroidetes were enriched in the IgA1$^-$ fraction (Fig. S5 E). Next, we used the same IgA1$^+$ EI to identify differences in the immune coating profile of fecal bacteria from UC patients and HCs. At the phylum level, no significant differences between UC patients and HCs were observed (Fig. S5 F). However, at the family level, the SIgA1-coated bacteria fraction from UC patients was enriched in the Erysipelotrichaceae family, which is potentially pathogenic (Kaakoush, 2015) (Fig. 7 J). This enrichment was further validated using the probability index proposed by Jackson et al. (2021) (Fig. 7 K).

We then analyzed gut bacteria from the mucus layer topping the intestinal mucosa of CD patients and found an increased frequency of mucus-embedded and SIgA1-coated bacteria in inflamed compared with non-inflamed segments of gut specimens from CD patients or non-IBD controls (Fig. 8 A). This increase was largely due to microbes dually coated by SIgA1 and SIgA2 (Fig. 8 B), which echoed our earlier findings from fecal samples of UC patients. Knowing that *E. coli* is a major player in CD immunopathogenesis (Manichanh et al., 2012; Pascal et al., 2017), we also analyzed the reactivity of intraluminal SIgA1 and SIgA2 to this pathobiont. Compared with mucus from non-IBD controls, mucus samples from inflamed gut segments of CD patients contained more abundant free SIgA (Fig. 8 C). This encompassed both SIgA1 and SIgA2, both of which strongly bound to *E. coli* (Fig. 8 D). By contrast, free SIgA1 and SIgA2 from non-IBD controls showed little or no binding to *E. coli* (Fig. 8 D).

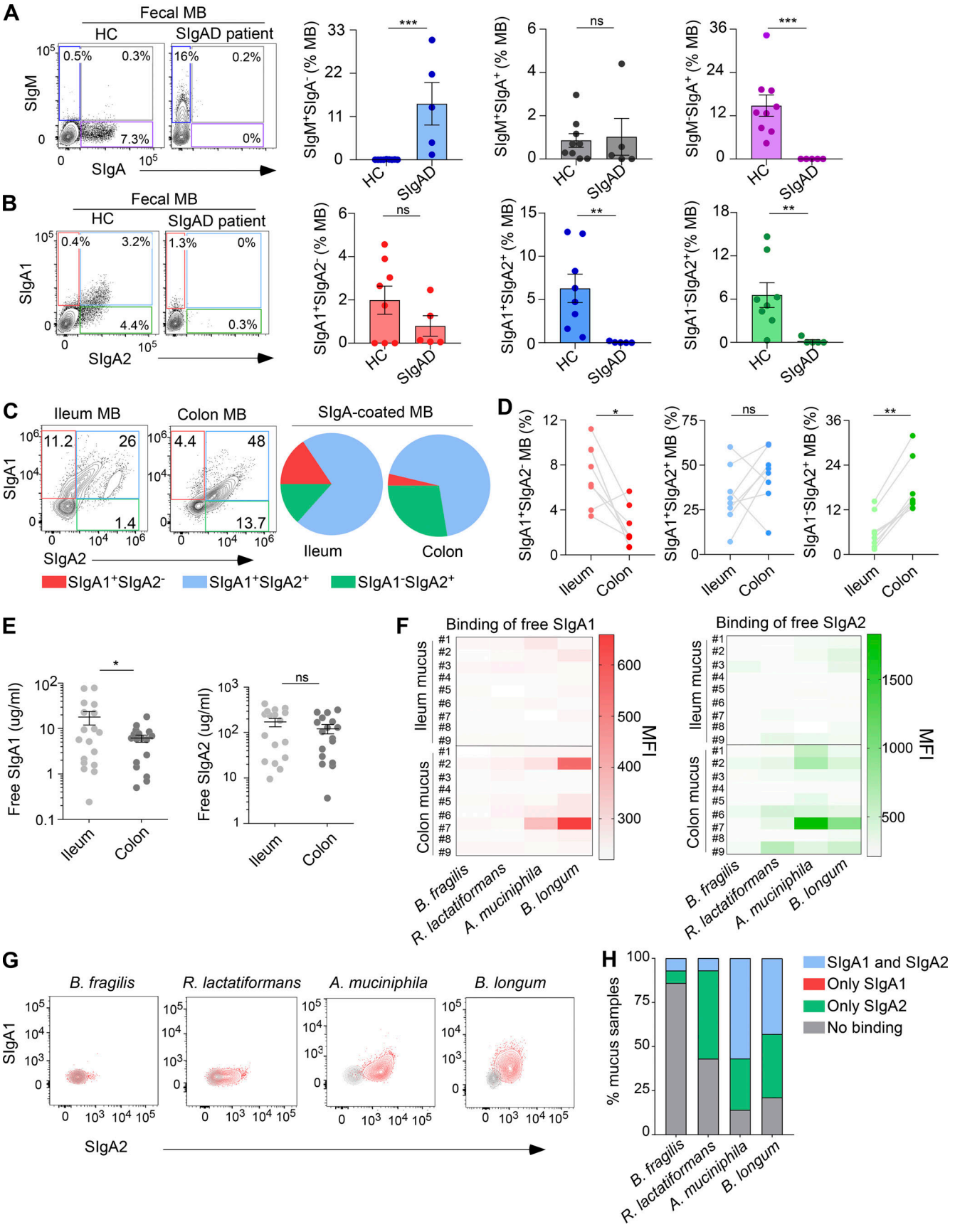

Figure 5. **Human intestinal SIgA2 mostly targets mucus-embedded bacteria dually coated by SIgA1. (A and B)** Representative FCA (left) and frequency of SIgM$^+$SIgA$^-$, SIgM$^+$SIgA$^+$, and SIgM$^-$SIgA$^+$ (A) or SIgA1$^+$SIgA2$^-$, SIgA1$^+$SIgA2$^+$, and SIgA1$^-$SIgA2$^+$ (B) SytoBC$^+$ fecal MB of HCs and SIgAD patients.

(C) Representative FCA (left) and summary pie charts (right) of mucus-embedded SIgA1$^+$SIgA2$^-$ (red), SIgA1$^+$SIgA2$^+$ (blue), and SIgA1$^-$SIgA2$^+$ (green) gut MB from histologically normal ileal or colonic gut segments. **(D)** Frequencies of mucus-embedded SIgA1$^+$SIgA2$^-$ (red), SIgA1$^+$SIgA2$^+$ (blue), and SIgA1$^-$SIgA2$^+$ (green) gut MB in ileal versus colonic gut segments. **(E)** Abundances of free SIgA1 (left) or free SIgA2 (right) in ileal versus colonic gut mucus secretions, measured by ELISA. **(F)** Heatmap visualization of the reactivity of free SIgA1 and free SIgA2 from terminal ileum or ascending colon for *B. fragilis*, *R. lactatiformans*, *A. muciniphila*, and *B. longum*. **(G)** Representative flow cytometric analysis of the reactivity of free SIgA1 and free SIgA2 for *B. fragilis*, *R. lactatiformans*, *A. muciniphila*, and *B. longum*. Red contour plots, viable SSC$^+$SytoBC$^+$ bacteria bound by free gut SIgA1 and/or SIgA2 from mucus supernatant and incubated with fluorochrome-labeled antibodies. Gray contour plots, control SSC$^+$SytoBC$^+$ bacteria incubated only with fluorochrome-labeled antibodies. **(H)** Bar plot showing the frequency of colonic mucus samples (n = 14) with the different binding profiles of free SIgA1 and free SIgA2. Positivity was defined as a 25% increase in MFI compared to negative controls, i.e., bacterial isolates incubated only with fluorochrome-labeled antibodies. Data summarize results from 9 (A) or 8 (B) HCs and 5 SIgAD patients (A and B), 8 (C and D), 18 or 17 (E, IgA1 and IgA2, respectively) or 9 (F) or 14 (H) samples. Error bars, SEM; two-tailed Mann–Whitney U test (A and B) and Wilcoxon matched paired test (D and E). *P < 0.05, **P < 0.01, ***P < 0.001.

Thus, gut homeostasis is characterized by a MB dually coated by SIgA1 and SIgA2, which is enriched in highly beneficial commensals such as *A. muciniphila*. Despite showing depletion of *A. muciniphila*, IBD features expansion of microbial communities dually coated by SIgA1 and SIgA2, with increased SIgA1 binding to potentially pathogenic commensals such as *E. coli* as well as members of the Erysipelotrichaceae family. These data suggest that gut inflammation alters the selection of gut microbes by SIgA1 and SIgA2 (Fig. 8 E).

Discussion

We have shown that gut IgA1$^+$ and IgA2$^+$ PCs display significant clonal relatedness and are enriched within short-lived CD19$^+$ PCs and long-lived CD19$^-$ PCs, respectively. These PCs release SIgA1 and SIgA2, which jointly coat a large fraction of mucus-embedded commensals. Disruption of homeostasis by IBD is associated with the expansion of actively proliferating IgA1$^+$ PBs, the decrease of long-lived IgA2$^+$ PCs, and the increase of SIgA1$^+$SIgA2$^+$ gut bacteria. Such changes are further associated with heightened SIgA1 targeting of potentially pathogenic bacteria like *E. coli* and members of the Erysipelotrichaceae family combined with a depletion of the dually coated beneficial commensal *A. muciniphila*. Altogether, our findings indicate that gut IgA1 and IgA2 predominantly emerge from clonally related PCs and undergo distinct changes in both frequency and reactivity during IBD.

IgA responses to gut microbes are viewed as a flexible adaptive immune strategy to establish a mutualistic relationship with the commensal MB (Macpherson et al., 2018; Chen et al., 2020; Seikrit and Pabst, 2021). While intestinal bacteria are key to gut IgA induction after birth (Hapfelmeier et al., 2010; Lindner et al., 2015; Planer et al., 2016), IgA–bacteria interactions shape the composition, topography, and immunometabolic functions of the gut MB (Chen et al., 2020; Macpherson et al., 2018; Nakajima et al., 2018; Kawamoto et al., 2012, 2014; Rollenske et al., 2021; Pabst and Slack, 2020; Sterlin et al., 2019, 2020). Despite recent advances (Sterlin et al., 2020; Kabbert et al., 2020; Uzzan et al., 2022), the ontogeny and reactivity of human IgA1 versus IgA2 in intestinal homeostasis and inflammation remain elusive.

We found that gut IgA1$^+$ and IgA2$^+$ PCs were absent during fetal life, but co-emerged as early as 6 wk after birth and progressively increased over the following 5 years. Notably, IgA2$^+$ PCs were more abundant than IgA1$^+$ PCs in distal gut segments. These results agree with earlier findings (Hapfelmeier et al., 2010; Planer et al., 2016) that post-natal human gut colonization by commensals leads to the emergence of IgA responses. By showing the simultaneous appearance of both IgA1$^+$ and IgA2$^+$ PCs soon after birth, our data indicate that the early postnatal intestinal mucosa is competent to generate the microenvironmental cues needed for the initiation of SIgA2 in addition to SIgA1 responses.

Gut IgA1$^+$ and IgA2$^+$ PCs exhibited largely comparable phenotypes. Yet, IgA2$^+$ PCs expressed more colon-homing GPR15 receptors than IgA1$^+$ PCs, which is consistent with the increased abundance of IgA2$^+$ PCs in the colonic mucosa. These data echo pioneering studies suggesting that protease-resistant IgA2 is more abundant than protease-sensitive IgA1 in the colon due to the heavier colonization of the colon by commensals compared to the proximal gut (Kett and Brandtzaeg, 1987). Compared with IgA1, IgA2 was enriched in intermediate CD19$^-$CD45$^+$ and late CD19$^-$CD45$^-$ PCs subsets, which are distinct from early CD19$^+$CD45$^+$ PCs (Landsverk et al., 2017). Given their ability to persist in the gut mucosa for decades (Landsverk et al., 2017; Jahnsen et al., 2018; Halliley et al., 2015), CD19$^-$ PCs may be more fit to establish long-lasting SIgA–MB interactions.

Dual SIgA1-SIgA2 responses targeted beneficial mucus-embedded commensals such as *A. muciniphila*, possibly to optimize their immune inclusion within the gut mucosa. This process would involve close cooperation of SIgA2 with SIgA1 through distinct but complementary structural and biochemical properties (Seikrit and Pabst, 2021; Chen et al., 2020). While SIgA2 with its protease-resistant short hinge region may be better equipped than SIgA1 to retain beneficial commensals within the protease-rich gut mucus layer, SIgA1 could optimize the anchoring of these commensals to mucus due to the unique glycosylation profile of its long hinge region (Woof and Russell, 2011; Chen et al., 2020).

By demonstrating the extensive clonal relationship of IgA2$^+$ PCs with IgA1 memory B and PC cells through both bulk and single-cell Ig V(D)J gene sequencing, our results together with additional evidence from earlier studies (Phad et al., 2022; King et al., 2021; Ellebrecht et al., 2018; Horns et al., 2016; Kitaura et al., 2017) indicate that gut IgA1$^+$ and IgA2$^+$ PC clones largely emerge from common gut naive B cell precursors. Moreover, data from Ig tree analysis and in vitro experiments suggests that a fraction of IgA2$^+$ clones could emerge from sequential IgA1-to-IgA2 CSR in addition to direct IgM-to IgA2-CSR.

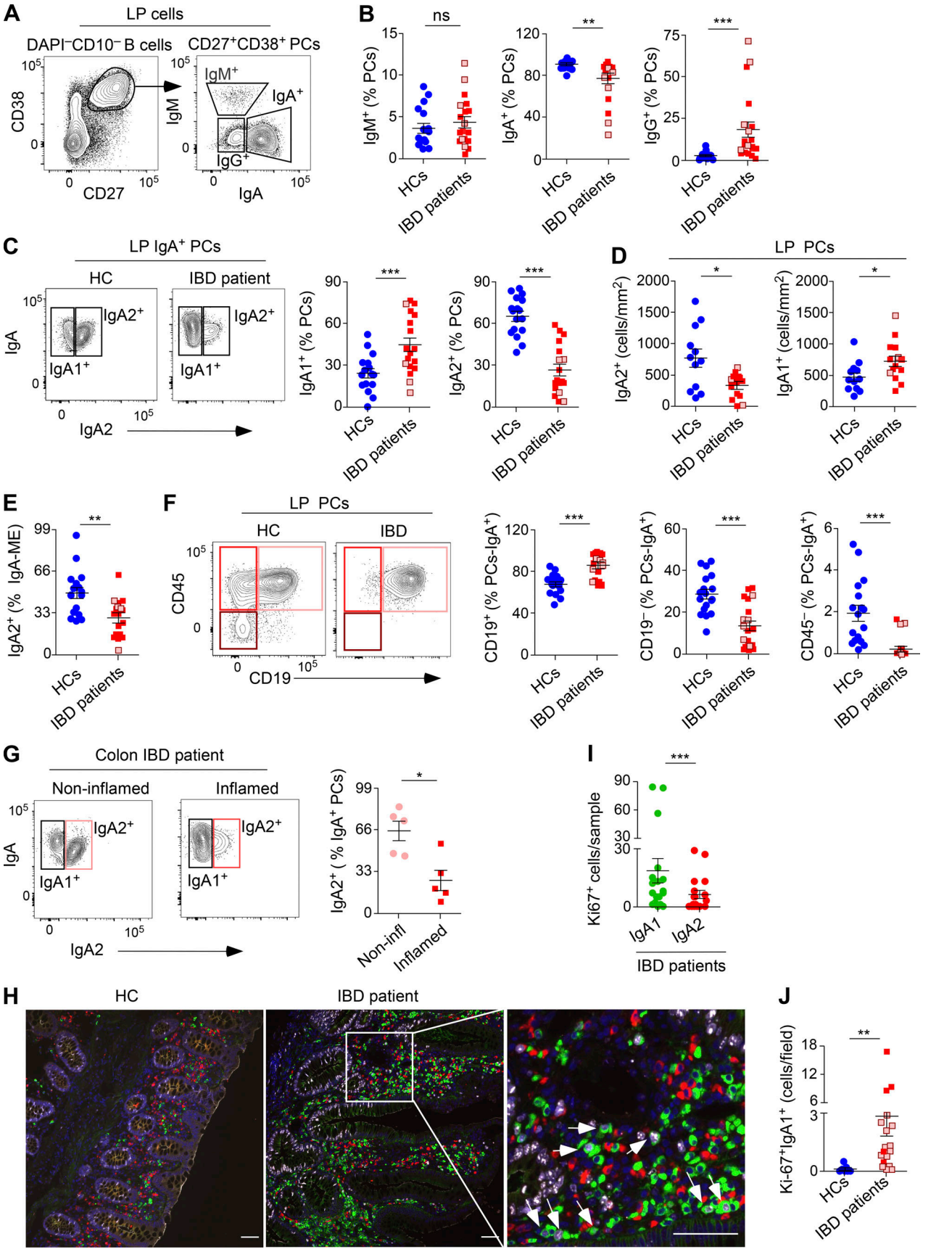

Figure 6. **Human gut inflammation elicits de novo induction of actively proliferating IgA1⁺ PBs while depleting late-stage IgA2⁺ PCs. (A and B)** FCA of CD38, CD27, IgA, and IgM expression on DAPI⁻CD10⁻ B cells from human colonic LP cells (A) and frequency of IgM⁺, IgA⁺, and IgG⁺ (defined as IgA⁻IgM⁻) PCs

from total colonic LP CD27$^+$CD38^{++}CD10$^-$ PCs of HCs and IBD patients (B). UC, bright red symbols; CD, open pink symbols. **(C)** FCA of IgA and IgA2 expression and frequencies of IgA1$^+$ (IgA$^+$IgA2$^-$) and IgA2$^+$ cells from colonic LP CD27$^+$CD38^{++}CD10$^-$ PCs from HCs and IBD patients. UC, bright red symbols; CD, open pink symbols. **(D)** IgA2$^+$ (left panel) and IgA1$^+$ (right panel) cells per mm^2 in colonic LP from HCs or IBD patients were calculated by tissue inspection through IFA. UC, bright red symbols; CD, open pink symbols. **(E)** FCA-derived frequencies of IgA2$^+$ cells within total colonic LP memory (ME) IgA$^+$ B cells from HCs and IBD patients. UC, bright red symbols; CD, open pink symbols. **(F)** FCA of CD45 and CD19 expression and frequencies of CD19$^+$, CD19$^-$, and CD45$^-$ PC subsets from colonic LP DAPI$^-$CD10$^-$CD27$^+$CD38^{++}IgA$^+$ PCs of HCs and IBD patients. UC, bright red symbols; CD, open pink symbols. **(G)** Representative FCA of IgA and IgA2 expression and percentage of IgA2$^+$ PCs on colonic LP IgA$^+$ PCs from both inflamed and non-inflamed gut segments from UC patients (n = 5). **(H)** IFA of IgA1 (green), IgA2 (red), Ki-67 (white), and nuclear DNA (blue) in gut LP from HC and IBD donors. Arrows point to actively proliferating IgA1$^+$Ki-67$^+$ PBs. Original magnification, 20×. Scale bars, 50 µm. **(I)** Frequencies of actively proliferating Ki-67$^+$ cells from total IgA1$^+$ or IgA2$^+$ PCs in gut LP from IBD patients. **(J)** Numbers of actively proliferating Ki-67$^+$IgA1$^+$ cells per microscopic field in gut LP from HCs and IBD patients. UC, bright red symbols; CD, open pink symbols. For each sample, 2–12 microscopic fields were analyzed. Data show one of more than three experiments yielding similar results (A, C left, F left, G, and I) or summarize results from at least 12 HCs and at least 14 IBD patients (B, C right graphs, D, E, F right graphs, and H) or from 7 HCs to 18 IBD patients (J). Error bars, SEM; Wilcoxon matched paired test (G and H) and two-tailed Mann–Whitney U test (B–F and J). *P < 0.05, **P < 0.01, ***P < 0.001. See also Fig. S4.

Sequential IgA1-to-IgA2 CSR likely occurs through intertwined follicular and extrafollicular pathways regulated by TD and/or TI signals. Indeed, IgA1$^+$ B cell precursors of IgA2$^+$ PCs expressed mutated IGHV genes, which implies that the initial transition from IgM to IgA1 was triggered by follicular TD signals. Instead, the transition from IgA1 to IgA2 was mostly uncoupled from de novo accumulation of IGHV gene mutations, and overall, gut IgA2$^+$ B cells did not harbor increased SHM compared with their IgA1 counterpart. Yet, the mutational load of shared IgA2$^+$, IgA1$^+$, and IgM$^+$ clones was significantly larger than the average mutational load of IgA2-only clones. This finding possibly reflects the need for memory IgM$^+$ or IgA1$^+$ B cells to undergo numerous transits through gut GCs to generate clonally affiliated IgA2$^+$ cells.

By analyzing overlapping IgA1 and IgA2 clones from elegantly separated GALT and GALT-free-LP material, a recent study (Fenton et al., 2020) found little evidence of sequential IgA1-to-IgA2 CSR in the gut LP. Due to our inability to fractionate IgA-expressing cells inhabiting gut follicles from IgA-expressing cells inhabiting the gut LP, we refrain from confirming or rejecting this conclusion. However, similar to our findings, the above study (Fenton et al., 2020) does suggest the partial overlapping of gut IgA1 and IgA2 clones. It must be also noted that the above study (Fenton et al., 2020) does not exclude the possibility that sequential IgA1-to IgA2 CSR could occur at gut inductive sites, including PPs. Clearly, more work is needed to fully address the frequency, topography, and modalities of IgA2 CSR events in the human gut mucosa.

Consistent with recently published data (Sterlin et al., 2020), SIgA1 coated a large fraction of gut commensals together with SIgA2. This finding suggests that the dual coating of gut commensals by SIgA1 and SIgA2 is instrumental to gut health. In agreement with a recent study (Rollenske et al., 2021), the shared antigen specificity of parallel SIgA1 and SIgA2 responses could be crucial to shape the fitness of a large fraction of the gut MB. Yet, our data suggest some SIgA2 may be also produced to exclusively target beneficial commensals such as *R. lactatiformans*, a *Ruminococcaceae* family member associated with gut homeostasis (Magri et al., 2017). Consistent with this possibility, a rare case of IgA2 deficiency has been recently associated with small bowel CD atypically targeting the duodenum (Canales-Herrerias et al., 2023).

Disruption of gut homeostasis by IBD was accompanied by the expansion of actively proliferating and short-lived IgA1$^+$ PBs combined with relative depletion of long-lived IgA2$^+$ PCs, particularly in inflamed gut segments. Similarly, IgG$^+$ PBs with reduced SHM and diversity are increased in the inflamed gut, together with an expansion of IFN-γ-imprinted naïve B cells (Uzzan et al., 2022; Martin et al., 2019; Castro-Dopico et al., 2019). Together these findings raise the possibility that IBD skews local humoral responses toward acute PB differentiation and proinflammatory IgG and IgA1 production. The precise mechanisms underpinning this skewing of the gut antibody response during IBD remain elusive, but inflammation-induced changes of microenvironmental signals from cytokines, chemokines, and metabolites involved in the regulation of B cell class switching, PC survival, and PC migration or retention might play an important role.

In addition to IgG, a type-1 inflammatory microenvironment could directly or indirectly enhance gut B cell production of IgA1 specific to most commensals while attenuating gut B cell production of IgA2 to certain microbes. Accordingly, the increased IgA1$^+$ and decreased IgA2$^+$ PC frequencies observed in IBD were accompanied by increased SIgA1 binding to potentially pathogenic commensals such as *E. coli* in CD patients. In UC patients, the above alterations were also associated with an enrichment of the SIgA1-coated fraction of Erysipelotrichaceae family members, which appears to contribute to gut inflammation (Manichanh et al., 2012; Kaakoush, 2015).

Concomitantly, IBD patients showed a depletion of *A. muciniphila*, a beneficial commensal physiologically coated by both SIgA1 and SIgA2. Altogether, our findings suggest that IBD perturbs bacteria selection by SIgA1 and SIgA2, fostering dominant gut SIgA1 responses that may promote the mucosal retention of pathogenic commensals as well as the enhancement of gut dysbiosis. The molecular background underpinning altered SIgA1 and SIgA2 reactivity in IBD remains unclear, but it has been recently proposed that altered MB binding by IgG from IBD patients stems from perturbed glycosylation, which in turn could result from altered IGHV gene somatic hypermutation (Huus et al., 2021; Simurina et al., 2018). We propose that similar mechanisms could alter the reactivity of SIgA1 and SIgA2.

In summary, we found that gut IgA1$^+$ and IgA2$^+$ PCs are clonally related and generate SIgA1 and SIgA2 responses that dually coat a large fraction of mucus-embedded bacteria, including beneficial commensals. Disruption of homeostasis by IBD is associated with the expansion of newly formed IgA1$^+$ PBs along with the depletion of late IgA2$^+$ PCs. These PC

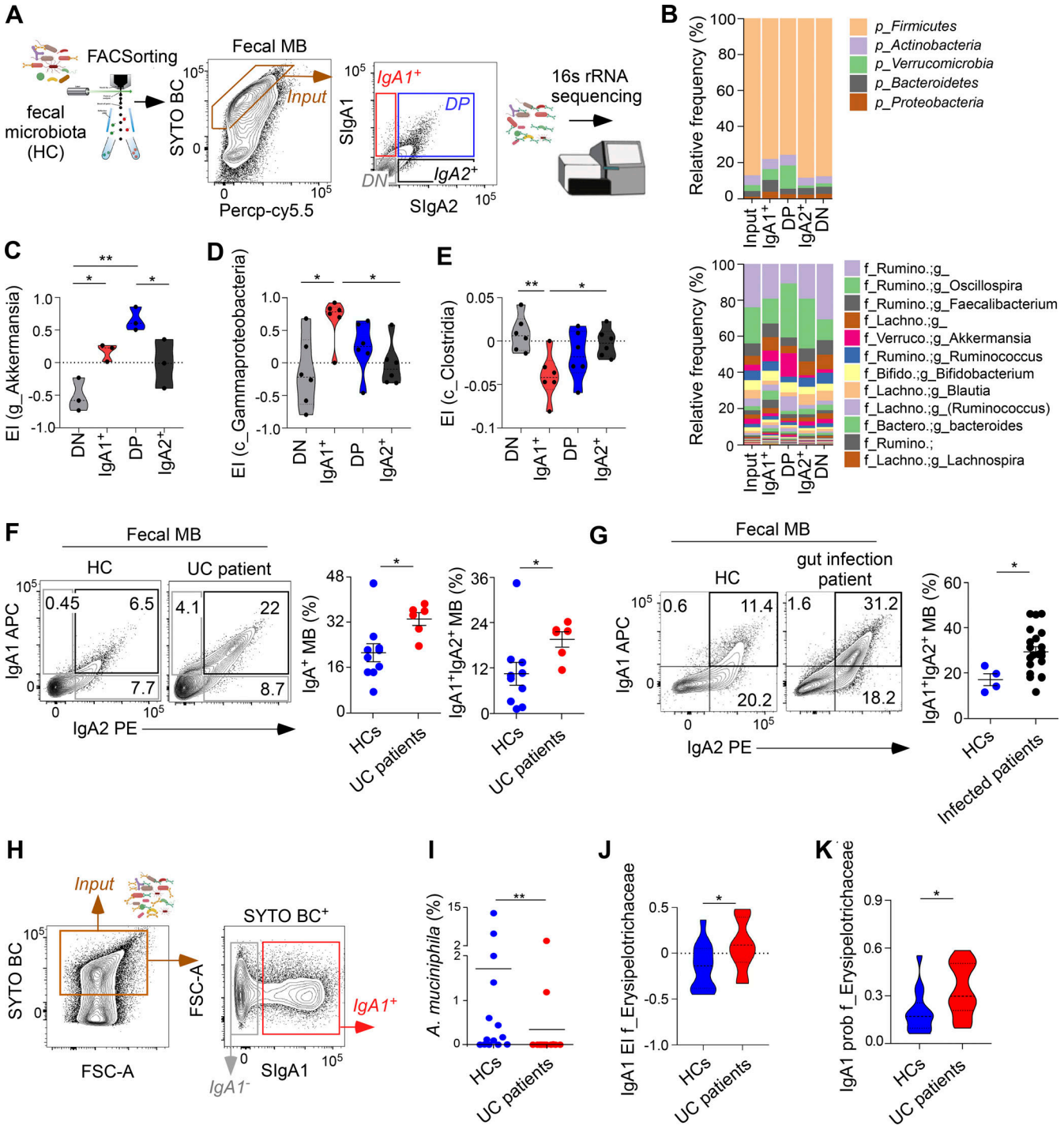

Figure 7. **Gut inflammation increases the frequency of intestinal bacteria dually coated by SIgA1 and SIgA2 and alters SIgA-mediated MB selection.** **(A)** Strategy adopted to profile the fecal MB from HCs and UC patients by 16S rRNA sequencing following SIgA1/SIgA2-based sorting of single positive SIgA1$^+$, single positive SIgA2$^+$, double-positive SIgA1$^+$SIgA2$^+$ (DP), and double-negative SIgA1$^-$SIgA2$^-$ (DN) bacteria. Total input SytoBC$^+$ bacteria were also sorted as control. **(B)** Relative abundance of phyla (upper panel) and genera (lower panel) in bacterial fractions sorted from the fecal MB of HC as in A. **(C–E)** EI for g_*A. muciniphila* (C), c_Gammaproteobacteria (D), and c_Clostridia (E) in bacterial fractions obtained from the fecal MB of HCs as in A. **(F and G)** FCA of SIgA1 and SIgA2 and frequencies of total SIgA$^+$ (SIgA1$^+$, SIgA1$^+$SIgA2$^+$, and SIgA2$^+$) or dually coated SIgA1$^+$SIgA2$^+$ (right panels) from SytoBC$^+$ fecal MB of HCs and patients with UC (F) or transient gastrointestinal infection (G) (see Table S2). **(H)** Strategy adopted to profile the fecal MB from HCs and UC patients by 16S rRNA sequencing following SIgA1-based sorting of SIgA1$^+$ bacteria, which include SIgA1$^+$ single positive and DP SIgA1$^+$SIgA2$^+$ bacteria. Total input SytoBC$^+$ bacteria were also sorted as control. **(I)** Relative abundance of *A. muciniphila* in the input fraction obtained from the fecal MB of HCs and patients with UC as in H. **(J and K)** IgA1 EI (J) and probability index (K) for f_*Erysipelotrichaceae* from the fecal MB of HCs and UC patients as in H. Data show one representative donor out of 6 (B), or 28 (H) or summarize the results of 6 HCs (C–E), 10 HC donors or 6 UC donors (F), 4 HC or 20 gut infection donors (G), 14 HC and UC donors (I–K). For each fecal sample, EI values were plotted only when a given bacteria was present in all fractions. Error bars, SEM (F and G); two-tailed Mann–Whitney *U* test (F, G, and I–K) and one-way ANOVA with Tukey's post hoc test (C–E); *P < 0.05, **P < 0.01. See also Fig. S5.

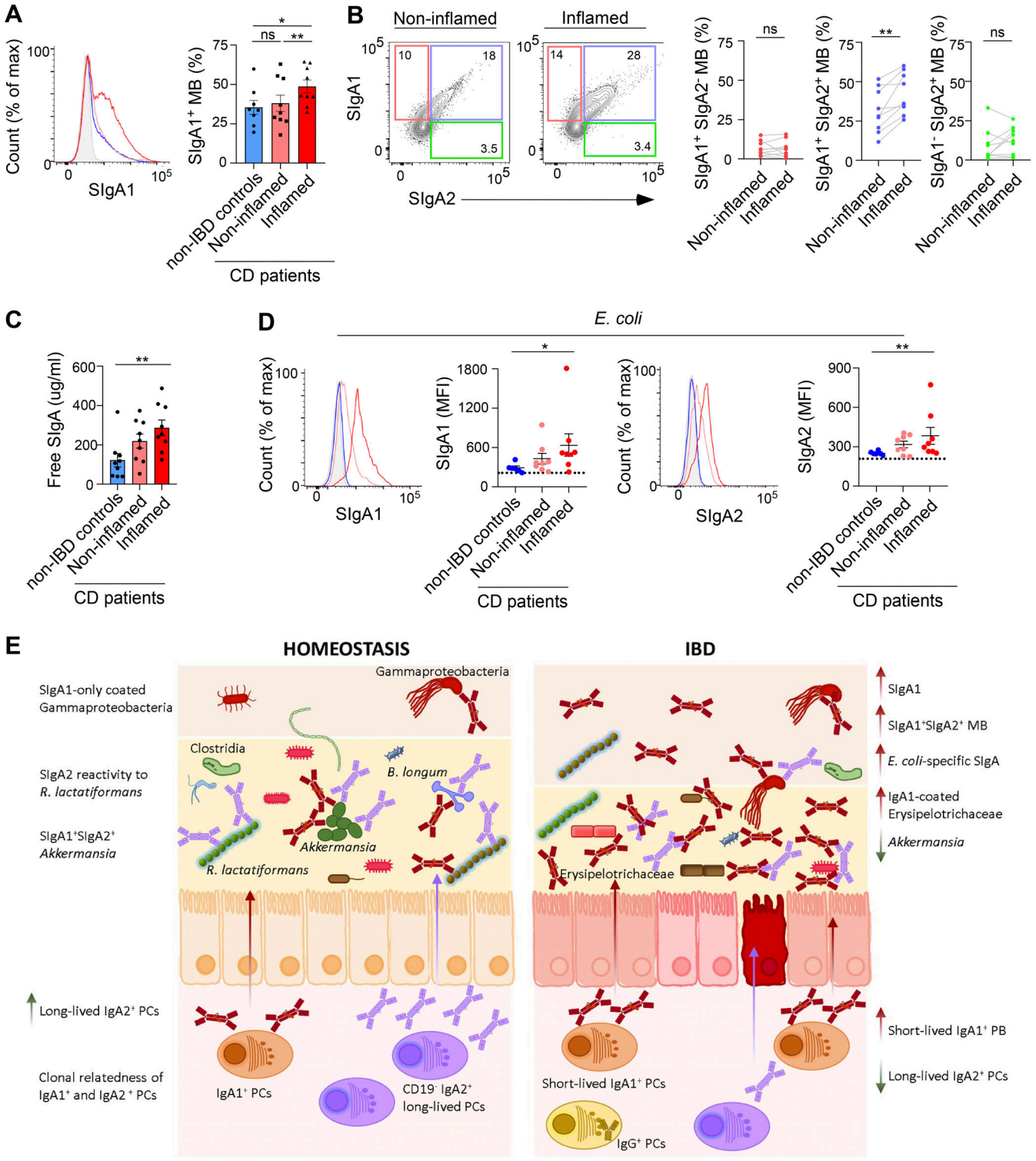

Figure 8. **IBD increases dual SIgA1 and SIgA2 coating of gut MB and augments SIgA1 and SIgA2 reactivity to *E. coli*. (A)** Representative flow cytometric profile (left) and frequencies (right) of SIgA1-bound mucus-embedded ileal MB from CD patients (red) and non-IBD controls (blue). CD samples included MB from inflamed (dark red) and non-inflamed (light red) segments of the gut mucosa. **(B)** Representative flow cytometry (left) and frequencies (right) of mucus-embedded SytoBC$^+$ gut bacteria, including SIgA1$^+$SIgA2$^-$ (red), SIgA1$^+$SIgA2$^+$ (blue), and SIgA1$^-$SIgA2$^+$ (green) bacteria inhabiting non-inflamed versus inflamed segments of the gut mucosa from CD patients. **(C)** ELISA of free SIgA from ileal mucus secretions of CD patients and non-IBD controls as in A. **(D)** Representative flow cytometric profiles and MFI of SIgA1 (left) and SIgA2 (right) bound to *E. coli*. SIgA1 and SIgA2 were obtained from gut mucus secretions of CD patients or non-IBD controls as in C and all samples were adjusted to a total IgA concentration of 10 µg/ml. **(E)** Schematic representation of proposed gut MB selection by SIgA1 and SIgA2 in homeostasis and IBD. In gut homeostasis, balanced IgA1 and IgA2 responses to the gut MB involve clonally related IgA1$^+$ and IgA2$^+$ PCs, including long-lived-enriched IgA2$^+$ PCs. These responses induce dual coating of intraluminal mucus-embedded commensal bacteria, including beneficial *A. muciniphila*, by SIgA1 and SIgA2 and preferential coating of *R. lactatiformans* and Gammaproteobacteria by SIgA2 and SIgA1, respectively. In IBD, the

expansion of short-lived IgA1+ PCs, including IgA1+ PBs, combined with the relative reduction of long-lived IgA2+ PCs associate with a global decrease of *A. muciniphila*, a general increase in dually coated bacteria, with increased SIgA1 binding to potentially pathogenic bacteria such as *E. coli* and members of the *Erysipelotrichaceae* family. Data summarize results from 8 non-IBD controls and 9 CD donors (A and B) or 9 non-IBD controls and 10 CD donors (C and D). SEM (A, C, and D); to compare non-IBD controls to IBD donors, two-tailed Mann–Whitney *U* test was used (A, C, and D); to compare noninflamed versus inflamed IBD segments, Wilcoxon matched paired test was used (A–D); *P < 0.05, **P < 0.01.

perturbations occur along with an altered selection of commensals by SIgA1 and SIgA2 and could contribute to the aggravation of gut dysbiosis. Based on these findings, we propose that the identification and functional characterization of microbial antigens specifically targeted by SIgA1 and SIgA2 may help develop novel treatments against IBD.

Materials and methods

Human tissue and blood specimens

Histologically normal tissue samples from the terminal ileum and ascending colon were obtained from 40 patients who underwent colonic surgery or right hemicolectomy due to colonic tumors, unresectable polyps, or angiodysplasia at Hospital del Mar, Barcelona (Spain). The age of these patients ranged from 30 to 83 years (mean: 66 years). Intestinal biopsies, formalin-fixed paraffin-embedded tissue sections, and blood were also obtained from 21 patients with UC (male/female ratio, 1.3; age from 21 to 69; mean age: 39.5), 7 CD patients (male/female ratio, 0.2; age from 21 to 67; mean age: 37.7), and 20 age-matched HCs (male/female ratio, 1.8; age ranged from 18.6 to 75; mean age 43.9) recruited from a cohort of patients followed at the Icahn School of Medicine at Mount Sinai (New York, NY, USA) and its affiliated hospitals and clinics. Fresh tissues and formalin-fixed and paraffin-embedded tissue sections were also collected from the Mar Biobanc (Barcelona, Spain), Sant Joan de Déu Hospital and Vall d'Hebron Hospital (Barcelona, Spain), and tissue repositories at Icahn School of Medicine at Mount Sinai with patient-signed informed consent (Table S1). All tissue samples were assigned coded identifiers and relevant clinical information remained concealed. Human splenocytes from histologically normal spleens were obtained from deceased organ donors or individuals undergoing posttraumatic splenectomy at Hospital del Mar, Barcelona. The use of blood and tissue samples was approved by the Ethical Committee for Clinical Investigation of the Institut Hospital del Mar d' Investigacions Mèdiques (CEIC-IMIM 2014/5892/I and 2018/8265/I), Vall d'Hebron Hospital (PR(AG)279/2023), and the Mount Sinai Institutional Review Board (HS#14-00174) with a patient or legal tutor signed informed consent.

Human fecal and mucus samples

Samples from all human MB donors (Tables S2 and 3) were labeled with a specific study identification (ID) number. Each of these samples was processed with no identifiers linked to it other than its study ID. The use of fecal MB samples was approved by the local Ethical Committee of the University Hospital Vall d'Hebron (Barcelona, Spain) and Istituto Microbiologico Cantonale (Bellinzona, Switzerland). Fecal samples were collected by the patient at home and brought to the hospital within 24 h and then stored at −80°C until processing. Mucus samples were collected from the Mar BioBanc at Hospital del Mar and their use was approved by the local Ethical Committee (CEIC-IMIM 2014/5892/I and 2018/8265/I) with patient-signed informed consent.

Processing of tissue samples

Intestinal tissue samples from patients undergoing right hemicolectomy were processed as follows. Briefly, gut mucosa and submucosa were dissected from muscularis externa and cut into 2–3-mm fragments. These tissue fragments were first washed in calcium and magnesium-free Hanks' balanced salt solution (HBSS) before incubation at 37°C for 20 min in HBSS supplemented with 5 mM dithiothreitol and 1 mM ethylenediaminetetraacetic acid (EDTA). Then, tissue fragments were transferred into a Falcon tube with 30 ml HBSS and shaken vigorously for 10 s twice. The supernatant, which contained the intraepithelial lymphocyte fraction, was discarded. The remaining fraction was digested by incubation for 40 min at 37°C with stirring in an HBSS solution supplemented with 1 mg/ml collagenase IV (Thermo Fisher Scientific), 50 ng/ml DNAse (New England Biolabs), and 0.5% human serum (Sigma-Aldrich). LP-derived suspensions were passed through a 70-µm filter, washed, and resuspended in RPMI 1640 medium (Thermo Fisher Scientific) with 10% fetal bovine serum (FBS). LP mononuclear cells were also isolated from gut biopsies obtained during colonoscopy. Some 8–12 biopsies were collected with forceps directly in an ice-cold RPMI medium. Biopsies were processed within 2 h of collection. They were transferred in 10 ml HBSS (Invitrogen) at pH 8 and with no Ca^{++} and Mg^{++}, but supplemented with 0.5 M EDTA and 1 M 4-(2-hydroxyethyl)-1-piperazineethanesulfonic acid (Lonza) and incubated for 20 min at 37°C. After thorough washes with HBSS, biopsies were placed in an RPMI solution supplemented with 0.5 µg/ml collagenase IV and DNAse I (Sigma-Aldrich) and digested by incubating them for 40 min at 37°C in a rotating incubator at 215 rpm. After physically disrupting them by pipetting up and down 10 times through a 25-gauge needle, tissue fragments from biopsies were sequentially filtered through 100-µm and 40-µm cell strainers and washed with RPMI medium twice. Human splenocytes were obtained from fresh splenic samples by enzymatic digestion of the tissue for 40 min at 37°C in HBSS solution supplemented with 1 mg/ml collagenase IV (Thermo Fisher Scientific), 50 ng/ml DNAse (New England Biolabs), and 0.5% human serum (Sigma-Aldrich), followed by separation on Ficoll-Hypaque gradient (GE Healthcare). Peripheral blood mononuclear cells were obtained from heparinized blood samples by separation on the Ficoll-Hypaque gradient (GE Healthcare).

Flow cytometry

Cells were incubated at 4°C with an FcR-blocking reagent (Miltenyi Biotec) before adding appropriate "cocktails" of the fluorochrome-

labeled monoclonal antibodies (mAbs) (Table S4). Dead cells were excluded through the use of 4′-6′-diamidine-2′-phenylindole (DAPI; Sigma-Aldrich). To stain intracellular BLIMP-1 and Ki67, the Cyto-Fast Fix/Perm Buffer Set (Biolegend) was used according to the manufacturer's instructions. Labeled cells were acquired with LSR Fortessa (BD Biosciences) and data were further analyzed with FlowJo V10 software (TreeStar).

Cell sorting

For cell sorting for the IGHV gene repertoire analysis, cell suspension was incubated at 4°C with FcR-blocking reagent (Miltenyi Biotec) and stained for 30 min with the following mAbs: anti-CD45 AF700 (clone HI30), anti-CD19 PE-Cy7 (clone HIB19), anti-CD10 PE (clone HI10a), anti-CD38APC-Cy7 (clone HIT2), anti-CD27 PercP-Cy5.5 (clone M-T271), anti-IgM BV605 (clone MHM-88), anti-IgD FITC (catalog number: 2032-02; Southern Biotech), and anti-IgA APC (clone IS11-8E10). Naïve $CD45^+CD19^+CD38^{dull}CD10^-IgD^{++}IgM^+CD27^-$ B cells, GC-IgM^+ $CD45^+CD19^+CD38i^{nt}CD10^+IgM^+$ and GC switched $CD45^+CD19^+CD38^{int}CD10^-IgM^-$ B cells, unswitched memory $CD45^+CD19^+CD38^{dull}CD10^-IgD^-IgM^+CD27^+$ B cells, memory class-switched $CD45^+CD19^+CD38^{dull}CD10^-IgD^-IgM^-CD27^+(IgA^+)$ B cells, unswitched $CD45^+CD19^+CD38^{++}CD10^-IgD^-IgM^+CD27^+$ PCs, and class-switched $CD45^+CD19^+CD38^{++}CD10^-IgD^-IgM^-CD27^+(IgA^+)$ PCs from terminal ileum and ascending colon from four different donors were sorted with a FACSAria II (BD Biosciences) after excluding dead cells by DAPI staining (Table S5). The purity of sorted cells was consistently >95%.

Immunomagnetic cell separation

IgD^+ and $IgA1^+$ B cells were magnetically sorted from human splenic and intestinal LP mononuclear cells, respectively. Human mononuclear cells were blocked at 4°C with an FcR-blocking reagent (Miltenyi Biotec) and then incubated for 15 min at 4°C with goat F(ab')2 anti-human IgD biotin or mouse anti-human IgA1 biotin (clone B3506B4; Southern Biotechnologies) antibodies, followed by 15 min incubation at 4°C with streptavidin microbeads (Miltenyi). Magnetically labeled cells were then purified using MACS LS columns placed in a MidiMACS Separator (Miltenyi). The purity of magnetically sorted cells was consistently >95% as determined by flow cytometry.

Cell cultures

Human IgD^+ and $IgA1^+$ B cells were seeded in 96-well U-bottomed plates (Thermo Fisher Scientific) and cultured for 6 days in complete RPMI 1640 medium (Biowest) supplemented with 10% FBS, penicillin (10 U/ml), and streptomycin (10 U/ml) with or without 100 ng/ml megaCD40L (Enzo Life Science) and 500 ng/ml IL-21 (Peprotech) (TD stimulation) or 1 µg/ml CpG ODN-2006 (Invivogen) (TI stimulation), supplemented with 50 ng/ml IL-10 (Peprotech), 0.01 ng/ml TGF-β (Peprotech), 500 ng/ml BAFF (Alexis), and 100 ng/ml Mega APRIL (Alexis) (IgA-inducing stimuli).

IFA

Formalin-fixed paraffin-embedded human tissue sections 3 µm in thickness were treated in xylene, a decreasing alcohol gradient, and distilled water to achieve de-waxing and rehydration of the tissue. Heat-induced epitope retrieval was performed for 15 min in citrate buffer (pH 6) or Tris-EDTA buffer (pH 9). After epitope retrieval, tissue sections were permeabilized with 0.2% Triton X-100 in PBS, blocked with 5% bovine serum albumin (BSA), and 5% Fc receptor blocking reagent (Miltenyi Biotec), and stained with various combinations of primary antibodies. These combinations included rabbit anti-human IgA1 (clone RM124, 1:500; Abcam), goat anti-human IgM at 1:50 dilution (cat. number: H15000; Invitrogen), mouse anti-human IgA2 at 1:50 dilution (clone IS11-21E11; Miltenyi), rabbit anti-human IgA at 1:1,000 dilution (cat. number: A0262; DAKO), rat anti-human/mouse Ki-67 at 1:50 dilution (clone SolA15; Thermo Fisher Scientific), and mouse anti-human CD138 at 1:30 dilution (clone: MI15; Agilent). Nuclear DNA was visualized with DAPI and coverslips were applied with FluorSave reagent (Merck Millipore). Images were acquired either with a Leica TCS SP5 Upright confocal microscope (Leica) or a Nikon Eclipse Ni-E microscope (Nikon) and processed with ImageJ software.

Sequencing of Ig gene repertoires

Total cellular RNA from sorted intestinal B cell subsets (Table S5) was isolated with the RNeasy Micro Kit (Qiagen) by following the manufacturer's protocol. About 2 ng of RNA was reverse transcribed into cDNA using TaqMan Reverse Transcription Reagents and random hexamers (Thermo Fisher Scientific). Aliquots of cDNA products (4 µl) were mixed in a total PCR volume of 25 µl with 50 nM primers purified by high-performance liquid chromatography and specific for the framework region 1 of VH1, VH2, VH3, VH4, VH5, or VH6, 250 nM primers specific for Cα, Cµ, or Cγ and encompassing corresponding Illumina Nextera sequencing tags along with molecular barcoding (Table S6), and high-fidelity platinum PCR supermix (Thermo Fisher Scientific).

Amplification was performed using the following conditions. An initial step of 95°C for 5 min was followed by 35 cycles including 95°C for 30 s, 58°C for 30 s, and 72°C for 30 s, supplemented with a final extension step of 72°C for 5 min. PCR products were purified with miniElute PCR purification Kit (Qiagen) and Nextera indices were added via PCR with the following conditions: 72°C for 3 min, 98°C for 30 s, five cycles of 98°C for 10 s, 63°C for 30 s, and 72°C for 3 min. Ampure XP beads (Beckman Coulter Genomics) were used to purify PCR products, which were subsequently pooled and denatured. Single-strand products were paired-end sequenced on a MiSeq instrument (Illumina) with the 600 Cycle v2 Kit (2 × 300 bp). In total, 10,182,511 IGHV gene sequences from four donors were obtained through HTS.

Ig gene repertoire analysis

Data preprocessing

Paired and raw sequencing reads were processed using pRESTO (Vander Heiden et al., 2014) version 0.5.8, removing reads with average Phred scores <20; masking (replacing by N's) V-region primers, removing C-region primers after both classes and subclasses were assigned using BLAST (Camacho et al., 2009) against a subclass database, to avoid false mutation detection and preserve gene length; using UMI to generate a single

consensus sequence for each UMI barcode for read 1 and read 2 separately, discarding sequences with UMI mismatch rates (relative to the UMI consensus) >0.1, sequences that do not share a common primer annotation with the majority of the UMI set were discarded, and read groups with ambiguous primer assignments; assembling paired-end consensus sequences into full-length Ig sequences; and removing duplicate nucleotide sequences that shared the same sub-isotype (Table S7).

Annotation, clonal assignment, and repertoire analysis

Sequences were annotated online using IMGT/HighV-QUEST version 3.4.15 (Brochet et al., 2008) with the IMGT/GENE-DB (Giudicelli et al., 2005) reference sequences from January 17, 2019. The IgA sub-class was identified using pRESTO's MaskPrimers.py script, which looks for an exact match (or a match up to a defined number or errors) in a user-defined orientation, and the following two 29-base primers: IGHA1: 5′-AGGCGATGACCACGTTCCCATCTGGCTGG-3′; IGHA2: 5′-ATGCGACGACCACGTTCCCATCTTGGGGG-3′. This identification was tested and found to be 99.93% accurate. VH gene usage was estimated for each donor and B cell subset and cells were grouped according to their correlation patterns by hierarchical clustering based on the Ward.D2 method. Using Change-O version 0.4.1 (Gupta et al., 2015), the annotated output was parsed, removing non-functional sequences from the database, determining the sequence similarity threshold for each patient dataset using a Change-O R script, and assigning the sequences into clones based on this threshold (Table S8). The clonal assignment was performed on the complete set of sequences received for each donor—that is, sequences from all tissue samples and populations (naïve and memory B cells and PCs). In total, 34,753, 34,694, 136,122, and 138,891 clones were analyzed from donors 1, 2, 3, and 4, respectively. Out of the latter, about a third—12,461, 12,993, 50,551, and 53,668 in Donors 1, 2, 3 and 4, respectively—were singletons, that is, clones with only one experimentally identified sequence, included in the study since they were verified with UMIs. Sampling depths were assessed by generating rarefaction curves using a custom R script. Clonal sharing between different isotypes or the cell subset was evaluated using in-house Python R scripts and plotted using the R package VennDiagrams (Chen and Boutros, 2011). Circos plots and bar plots were designed using R (v4.3.1) with the packages circlize (v0.4.16) and ggplot2 (v3.5.1). For Circos plot analysis, a rarefied sample of a maximum of 10,000 sequences per subset was used to account for possible sample size biases between donors, tissues, and cell types. Repertoire diversity profiling (Greiff et al., 2015) was performed using the Immcantation tool alphaDiversity (Gupta et al., 2015). We considered a V(D)J clone to be mutated when harboring more than two mutations since the PCR step might be responsible for 1–2 mutations per clone (Hendricks et al., 2019). SHM levels were estimated by averaging the number of mutations compared to the inferred germline sequence of each clone belonging to a given B cell subset and donor.

Ig gene lineage-tree–based analysis

Lineage trees were constructed using IgTree, and the resulting trees were analyzed using an in-house Java program, PopTree, written by Sarai Zada, Nir Wolf, and Alina Boruhov under the guidance of Lena Hazanov, Miri Michaeli, and Prof. Ramit Mehr. In total, 34,648, 34,514, 114,749, and 90,795 lineage trees were created from the data of Donors 1, 2, 3, and 4, respectively. PopTree measures many aspects of B cell population relationships, such as the average level at which a certain population is located on the trees, the degree of population mixing in trees, the locations of key mutations, and more. We defined a "transition" on a clonal lineage tree as a path, down a branch of the tree, leading from a sequence representing a cell from one subset, e.g., MBc, to another, e.g., a PC sequence. PopTree counts the transitions between pairs of populations in the trees, and the numbers of mutations along these transitions. Further analyses used IgTreeZ (Neuman et al., 2022), a program that incorporates PopTree, MTree—a lineage tree topology measurement program (Shahaf et al., 2008), a comprehensive mutation analysis module (see below), selection analysis based on the focused binomial test (Hershberg et al., 2008), lineage tree filtering by user-chosen features, and lineage tree drawing. Overall, 530,051 transitions were surveyed in the course of our analysis. Mutations in each experimentally identified sequence were also counted on clonal lineage trees along the path from the tree root to each sequence in the same manner as we count mutations over transitions. Counts were performed on all the lineage trees in each donor's repertoire and then averaged for all the sequences in each B cell population/tissue/isotype sequence group.

Cell isolation, single-cell RNA, and V(D)J-seq library preparation, sequencing, and analysis

Gut LP cells from one histologically normal ileal gut tissue were processed as previously described and stained with DAPI. Viable cells (DAPI–) were sorted with a FACSAria II (BD bioscience) for 5′single-cell RNA and V(D)J sequencing using the Chromium10x Genomics platform (10x Genomics). Around 16,000 viable cells were loaded for sequencing analysis. Generation of gel beads in emulsion (GEMs), barcoding, and GEM-reverse transcription were performed using the Chromium Single Cell 5′ and V(D)J Reagent Kits (10x Genomics) according to the manufacturer's instructions. Sequencing was done on a NovaSeq 6000 S2 platform (Illumina). Sequences were preprocessed using the CellRanger 7.1.0 software pipeline (10x Genomics) with 98% of cells with a productive V-J spanning pair. Singularity shell from the Immcantation Framework (v.4.4.0) (http://immcantation.org) was used to analyze sequencing data with Change-O (v.1.3.0) (Gupta et al., 2015). Data preprocessing involved annotating filtered_contig.fasta files using reference V(D)J germline sequences in the container and converting them to AIRR format with IgBlast (Ye et al., 2013). Non-productive sequences, cells with multiple heavy chains, and cells without heavy chains were excluded. Cluster thresholds were calculated using the SHazaM package (v.1.1.2) (Gupta et al., 2015) and clones were defined using hierarchicalClones (only_heavy = TRUE) from the scoper package (v.1.2.1) (Nouri and Kleinstein, 2020). Germline sequences for heavy chains were created using the dowser package (v.1.1.1) (Hoehn et al., 2021). Somatic hypermutation in the V gene was calculated with observedMutations function from ShazaM, and clones were formatted using formatClones

function from dowser. Lineage trees were constructed using getTrees function (collapse = TRUE) from dowser. Honeycomb plots were generated with the enclone tool (v.0.5.219) (10x Genomics) using the raw json files input data.

Mucus and feces collection and processing

Mucus was obtained by scraping off the epithelial surface of macroscopically unaffected fresh tissue samples from the terminal ileum and ascending colon of patients undergoing right hemicolectomy. Aliquots of microbial samples from mucus or fecal samples were weighed and resuspended at 100 or 50 mg/ml, respectively, in PBS with protease inhibitors from SIGMA-FAST protease inhibitor tablets (Sigma-Aldrich). Mucus samples were homogenized by vigorous vortexing for 5 min and then centrifuged at 400 *g* for 5 min to pellet large debris. Homogenized fecal samples were allowed to sediment by gravity for 5–10 min at 4°C, and clarified fecal suspensions were centrifuged to pellet any remaining debris. The resulting supernatant was filtered through a sterile 70-µm cell strainer and centrifuged at 8,000 *g* for 5 min to pellet microbes. At this stage, supernatants were saved and frozen at −80°C to allow subsequent measurements of bacteria-free SIgA1 and SIgA2 by ELISA. Microbial pellets were used to perform bacterial flow cytometry and sorting.

ELISAs

To measure IgA, IgA1, and IgA2, 96-well ELISA plates (Thermo Fisher Scientific) were coated overnight at 4°C with goat anti-human Ig (polyclonal, cat. 2010-01; Southern Biotech), mouse anti-human-IgA1 (clone B3506B4), and anti-IgA2 (clone 14AS) mAbs (Abcam), respectively at 1 µg/ml in carbonate–bicarbonate buffer. Plates were blocked with 5% BSA for 2 h at room temperature and serial dilutions of supernatants from processed intestinal mucus samples were added and incubated for 2 additional hours. Then, for total IgA, plates were incubated with horseradish peroxidase–conjugated anti-human IgA secondary antibody (Southern Biotech) diluted 1:4,000 in PBS-Tween-20 supplemented with 1% BSA for 45 min at room temperature. For IgA1 and IgA2, biotin-labeled mouse mAbs to human IgA1 or human IgA2 (clones B3506B4 and A9604D2; Abcam, respectively) were added at 0.5 µg/ml for 1 h, followed by incubation with 1 µg/ml peroxidase-conjugated streptavidin (Vector Laboratories) for 45 min. 5,5′-Tetrametil-benzidina (TMB) substrate reagent set (BD Bioscience) was added until standard saturation and the reaction was stopped with 1 M H_2SO_4. OD_{450} was measured and antibody concentrations were calculated after background subtraction.

Bacterial flow cytometry and sorting

To measure endogenous SIgM, SIgA, SIgA1, and SIgA2 bound to intestinal bacteria, fecal pellets or mucus samples were resuspended in PBS and incubated for 30 min on ice with the following antibody combinations: anti-human IgM APC (clone SA-DA4; Southern Biotech) and anti-human IgA PE (Miltenyi Biotec) or anti-human IgA1 AF647 (clone B3506B4; Southern Biotech) and anti-human IgA2 PE (clone IS11-21E11; Miltenyi). Finally, bacterial samples were washed and resuspended in PBS with SYTO BC (1:4,000; Thermo Fisher Scientific) for 15 min on ice to perform bacterial flow cytometry. Contamination was minimized by passing all buffers and media through sterile 0.22-µm filters before use and working under a sterile hood. Bacterial flow cytometry was performed using a FORTESSA Cytometer (BD Bioscience) or with the Cytek Aurora Cytometer (Cytek Bioscience) with low forward scatter (FSC) and side scatter (SSC) thresholds to allow bacterial detection. FSC and SSC were set to a log scale and samples were gated FSC^+SSC^+SYTO BC^+ PercP $cy5.5^{-/low}$ and then assessed for SIgA and SIgM or SIgA1 and SIgA2 staining. Microbial samples from human feces were sorted using a FACSAria II (BD Biosciences) instrument with an 85-µm nozzle to minimize contamination (Jackson et al., 2021). Threshold settings were set to the minimal allowable voltage for SSC and 50,000 events were collected from the input and bacterial $SIgA1^-SIgA2^-$, $SIgA1^+SIgA2^-$, $SIgA1^+SIgA2^+$, and $SIgA1^-SIgA2^+$ fractions or bacterial $SIgA1^+$ and $SIgA1^-$ fractions were established according to a specific gating strategy (Fig. 7, A and H, respectively). Each enriched fraction (typically 50 µl) was sorted (purity >80%) and stored at −80°C before performing PCR and sequencing of bacterial 16S rDNA. Multiple precautions were taken to minimize potential contamination of sorted bacterial fractions, including collecting samples from the flow cytometer droplet stream (sheath fluid) immediately before and after each sorting to allow assessment of any potential contaminants in fluid lines.

In all experiments involving bacterial flow cytometry and bacterial FACSorting, mucus or fecal samples were also stained with isotype controls (anti-human CD3 AF647 [clone UCHT1; Southern] and anti-human CD117 PE [A3C6E2; Miltenyi]) to guide the specific gating strategies. The isotype controls were fluorescently labeled, came from the same species, and were at the same concentration as the anti-Ig antibodies used for the analysis.

Bacterial 16S rRNA gene analysis

16S rRNA amplicons from sorted bacteria were generated by adding 2.5 µl of each bacterial fraction directly into the Platinum PCR SuperMix High Fidelity (Thermo Fisher Scientific) solution, which contains PCR primers that target bacterial 16S V3 and V4 regions (Table S6) in triplicate 20-µl reactions. 16S rRNA analysis was also performed with samples collected from the flow cytometer droplet stream before every sort (sheath fluid), which permitted the identification of contaminant sequences that did not originate from the sorted sample. The following PCR conditions were used: an initial denaturation step at 95°C for 10 min was followed by 35 cycles that included 95°C for 30 s, 55°C for 30 s, and 72°C for 30 s, with an ending step of 72°C for 5 min. Triplicate reactions were pooled and subjected to 1% agarose gel electrophoresis to identify correct PCR products. These gels also included lanes with aliquots from negative control reactions. Pooled amplicons were purified with AMPure XP magnetic beads (Agencourt) and subjected to multiplexed sequencing on a MiSeq instrument (Illumina) with the 500 Cycle V2 Kit (2 × 250 bp). QIIME2 (v2019.1, [Bolyen et al., 2019]) was used to execute the whole 16S analysis. Paired-end 250 nucleotide reads were filtered using dada2 (Callahan et al., 2016), and

the sequences obtained were grouped into a phylogenetic tree. Those sequences were identified using the Greengenes database (version 13_8, 97%_otus). Similar to sorted fractions, sheath fluid samples were sequenced and processed to identify putative contaminant operational taxonomic units (OTUs). A comparison against "high-biomass" samples (fecal samples) was performed to identify the most frequent contaminant OTU detected in the sheath fluid but not high-biomass samples. The more abundant OTU sequences in the sheath fluid (>1,000 counts) were excluded from all the samples. Rarefied α diversity plots for Shannon Index and Phylogenetic Diversity (PD_whole_tree) were generated using default QIIME2 scripts, randomly subsampling each sample to 64,800 counts. An EI was calculated for each OTU (OTU_S present in three or more input samples): EI = Log 10 ([OTU% in SIgN]/OTU % in input). As confirmation, we also measured the probability index (Jackson et al., 2021) using the provided pipeline (https://cran.r-project.org/web/packages/IgAScores/vignettes/IgAScores.html).

Bacterial reactivity of secreted Igs from mucus

To measure the reactivity of free SIgA1 and SIgA2 from ileal and colonic mucus samples, supernatants from the bacterial pellet (obtained from mucus as previously described) were centrifuged at 16,000 *g* for 30 min at 4°C and were then filtered through 0.22-µm filters. The reactivity was measured against 10^5–10^6 heat-inactivated bacterial isolates (65C for 20 min) of the following species: *E. coli* (25992; ATCC), *Bacteroidetes fragilis* (25285; ATCC), *B. longum* (15707; ATCC), *Ruthenibacterium lactatiformans* (100348; ATCC), *and Akkermansia municiphila* (MBD0006; Sigma-Aldrich). Free Igs and bacteria were incubated for 30 min at RT. After washing, bacterial pellets were incubated for 15 min at RT with the secondary antibodies anti-human IgA1 AF647 (clone B3506B4; Southern Biotech) and anti-human IgA2 PE (clone IS11-21E11; Miltenyi). Finally, bacterial samples were washed and resuspended in PBS with SYTO BC (1:60,000; Thermo Fisher Scientific) to perform bacterial flow cytometry. Contamination was minimized by passing all buffers and media through sterile 0.22-µm filters before use. For each bacterial isolate analyzed, a control tube without SIg-containing supernatants was included to define non-specific binding of secondary antibodies. Bacterial flow cytometry was performed using a Cytek Aurora Cytometer (Cytek Bioscience) with low FSC and SSC thresholds to allow bacterial detection. FSC, SSC, and SYTO BC were set to a log scale and samples were gated $SSC^+SYTO\ BC^+$ and then assessed for SIgA1 and SIgA2 staining.

Quantification and statistical analysis

Differences between means from independent groups were assessed using Prism 5.03 software (GraphPad) and R studio. Samples were tested for normality, and parametric or non-parametric statistical tests were applied according to their distribution. For comparisons between two groups, P values were determined by unpaired or paired two-tailed Student's *t* test (parametric), two-tailed Mann–Whitney *U* test, or Wilcoxon matched paired test (non-parametric) as indicated. For comparisons between more than two groups, significance was calculated by one-way ANOVA with Tukey's post-hoc test (parametric) or with the Kruskal–Wallis test (non-parametric) as indicated. P values <0.05 were considered significant (*P < 0.05, **P < 0.01, ***P < 0.001).

Online supplemental material

Fig. S1 shows the phenotypic analysis of intestinal and circulating B cells and PCs by high-dimensional flow cytometry. Fig. S2 depicts the repertoire and lineage tree features. Fig. S3 reports Ig repertoire analysis of intestinal B cells after clonal grouping. Fig. S4 shows the phenotypic analysis of circulating and intestinal B cells from HCs and UC patients by high-dimensional flow cytometry. Fig. S5 shows the composition of fecal bacteria from HCs and UC patients as determined by 16S rRNA sequencing. Table S1 lists the tissue and blood samples studied through flow cytometry or immunofluorescence microscopy, including some key parameters of their donors. Table S2 lists the stool specimens analyzed by 16S rRNA sequencing, including some key parameters of their donors. Table S3 lists the intestinal mucus samples analyzed by FCA. Table S4 lists the antibodies used to perform flow cytometry, immunofluorescence microscopy, and ELISA. Table S5 lists the populations and numbers of cells sorted to perform high-throughput Ig gene repertoire analysis. Table S6 lists the primers used to perform high-throughput next-generation sequencing. Table S7 shows the number of IGHV sequences that have passed each stage of the preprocessing. Table S8 shows the numbers of IGHV sequences that have passed IMGT and filtering for functional sequences as well as the number of clones and threshold for their assignment.

Data availability

Ig gene and 16s RNA sequencing data are publicly available at NCBI's Sequence Read Archive, accession codes PRJNA596067 and PRJNA902959, respectively. Raw and processed sequencing reads of scRNA and V(D)J-seq are available in Gene Expression Omnibus under accession number GSE268929. Mehr lab scripts mentioned in the section on lineage tree-based analysis are available from Hadas Neuman (hadas.doron@gmail.com) or Ramit Mehr (Ramit.Mehr@BIU.ac.il) upon request. All other data supporting the findings of this study are available within the article and its supplementary information files. Materials and correspondence: Further information and requests for resources and reagents should be directed to and will be fulfilled by the lead contacts, Andrea Cerutti (acerutti@researchmar.net) and Giuliana Magri (gmagri@ub.edu).

Acknowledgments

We thank the Genomic core Facility from Pompeu Fabra University and the Single Cell Genomics unit from CNAG for assistance with high-throughput sequencing and the FACS unit from Pompeu Fabra University and Center of Genomic Regulation for help in cell sorting.

This work was funded and supported by Ministry of Economy and Competitiveness grant RTI2018-093894-B-I00, U.S. National Institutes of Health grants P01 AI61093 (to A. Cerutti) and R01 DK 112296-01 (to A. Cerutti and S. Mehandru), U.S.-

Israel Binational Science Foundation grant 2013432 (to R. Mehr), Crohn's & Colitis Foundation of America career development award 877970 (to E.K. Grasset), Grant Miguel Servet research program MS19/0002, grant RYC2021-031642-I, grant CNS2023-144474, and grant PID2023-148826OB-I00 by the Spanish Ministry of Science and Innovation and European Fund for Regional Development (to G. Magri), and grant FIS PI21/00037 from Instituto de Salud Carlos III (to G. Magri and L. Márquez-Mosquera).

Author contributions: S. Tejedor Vaquero: Formal analysis, Investigation, Methodology, Validation, Writing - original draft, Writing - review & editing, H. Neuman: Data curation, Formal analysis, Investigation, Methodology, Software, Writing - original draft, L. Comerma: Conceptualization, Formal analysis, Investigation, Validation, Visualization, Writing - review & editing, X. Marcos-Fa: Data curation, Formal analysis, Investigation, Methodology, Visualization, Writing - original draft, C. Corral-Vazquez: Formal analysis, Visualization, M. Uzzan: Investigation, Validation, Writing - review & editing, M. Pybus: Formal analysis, D. Segura-Garzón: Methodology, J. Guerra: Conceptualization, Formal analysis, Investigation, Methodology, L. Perruzza: Investigation, Resources, R. Tachó-Piñot: Investigation, J. Sintes: Investigation, A. Rosenstein: Investigation, E.K. Grasset: Investigation, Writing - review & editing, M. Iglesias: Resources, M. Gonzalez Farré: Resources, Writing - review & editing, J. Lop: Resources, Writing - review & editing, M.E. Patriaca-Amiano: Resources, M. Larrubia-Loring: Resources, P. Santiago-Diaz: Resources, J. Perera-Bel: Formal analysis, Software, Visualization, P. Berenguer-Molins: Formal analysis, Software, Writing - review & editing, M. Martinez Gallo: Resources, Visualization, A. Martin-Nalda: Resources, E. Varela: Investigation, M. Garrido-Pontnou: Investigation, Resources, Supervision, F. Grassi: Investigation, Resources, Supervision, Validation, F. Guarner: Resources, Validation, S. Mehandru: Conceptualization, Investigation, L. Márquez-Mosquera: Investigation, Resources, Writing - review & editing, R. Mehr: Data curation, Formal analysis, Investigation, Methodology, Software, Supervision, Visualization, Writing - original draft, Writing - review & editing, A. Cerutti: Conceptualization, Funding acquisition, Project administration, Resources, Supervision, Validation, Writing - original draft, Writing - review & editing, G. Magri: Conceptualization, Data curation, Formal analysis, Investigation, Methodology, Project administration, Supervision, Validation, Visualization, Writing - original draft, Writing - review & editing.

Disclosures: L. Comerma reported personal fees from Roche, MSD, AstraZeneca, and Diaceutics and non-financial support from Roche, MSD, AstraZeneca, and Phillips outside the submitted work. M. Iglesias reported personal fees from Bristol Myers Squibb, Merck Sharp & Dohme, Roche, Astellas, Merck, Agilent, and Seagen outside the submitted work. No other disclosures were reported.

Submitted: 12 January 2023
Revised: 13 June 2024
Accepted: 24 September 2024

References

Ansaldo, E., L.C. Slayden, K.L. Ching, M.A. Koch, N.K. Wolf, D.R. Plichta, E.M. Brown, D.B. Graham, R.J. Xavier, J.J. Moon, and G.M. Barton. 2019. Akkermansia muciniphila induces intestinal adaptive immune responses during homeostasis. *Science*. 364:1179–1184. https://doi.org/10.1126/science.aaw7479

Barak, M., N.S. Zuckerman, H. Edelman, R. Unger, and R. Mehr. 2008. IgTree: Creating immunoglobulin variable region gene lineage trees. *J. Immunol. Methods*. 338:67–74. https://doi.org/10.1016/j.jim.2008.06.006

Berkowska, M.A., G.J.A. Driessen, V. Bikos, C. Grosserichter-Wagener, K. Stamatopoulos, A. Cerutti, B. He, K. Biermann, J.F. Lange, M. van der Burg, et al. 2011. Human memory B cells originate from three distinct germinal center-dependent and -independent maturation pathways. *Blood*. 118:2150–2158. https://doi.org/10.1182/blood-2011-04-345579

Bolyen, E., J.R. Rideout, M.R. Dillon, N.A. Bokulich, C.C. Abnet, G.A. Al-Ghalith, H. Alexander, E.J. Alm, M. Arumugam, F. Asnicar, et al. 2019. Reproducible, interactive, scalable and extensible microbiome data science using QIIME 2. *Nat. Biotechnol.* 37:852–857. https://doi.org/10.1038/s41587-019-0209-9

Brandtzaeg, P., I.N. Farstad, F.E. Johansen, H.C. Morton, I.N. Norderhaug, T. Yamanaka, P. Brandtzaeg, I.N. Farstad, F. Johansen, H.C. Morton, et al. 1999. The B-cell system of human mucosae and exocrine glands. *Immunol. Rev.* 171:45–87. https://doi.org/10.1111/j.1600-065X.1999.tb01342.x

Brochet, X., M.P. Lefranc, and V. Giudicelli. 2008. IMGT/V-QUEST: The highly customized and integrated system for IG and TR standardized V-J and V-D-J sequence analysis. *Nucleic Acids Res.* 36:W503–W508. https://doi.org/10.1093/nar/gkn316

Bunker, J.J., T.M. Flynn, J.C. Koval, D.G. Shaw, M. Meisel, B.D. McDonald, I.E. Ishizuka, A.L. Dent, P.C. Wilson, B. Jabri, et al. 2015. Innate and adaptive humoral responses coat distinct commensal bacteria with immunoglobulin A. *Immunity*. 43:541–553. https://doi.org/10.1016/j.immuni.2015.08.007

Callahan, B.J., P.J. McMurdie, M.J. Rosen, A.W. Han, A.J.A. Johnson, and S.P. Holmes. 2016. DADA2: High-resolution sample inference from Illumina amplicon data. *Nat. Methods*. 13:581–583. https://doi.org/10.1038/nmeth.3869

Camacho, C., G. Coulouris, V. Avagyan, N. Ma, J. Papadopoulos, K. Bealer, and T.L. Madden. 2009. BLAST+: Architecture and applications. *BMC Bioinformatics*. 10:421. https://doi.org/10.1186/1471-2105-10-421

Canales-Herrerias, P., Y. Garcia-Carmona, J. Shang, H. Meringer, D.S. Yee, L. Radigan, S. Buta, G. Martinez-Delgado, M. Tankelevich, D. Helmus, et al. 2023. Selective IgA2 deficiency in a patient with small intestinal Crohn's disease. *J. Clin. Invest.* 133:e167742. https://doi.org/10.1172/JCI167742

Caruso, R., B.C. Lo, and G. Núñez. 2020. Host–microbiota interactions in inflammatory bowel disease. *Nat. Rev. Immunol.* 20:411–426. https://doi.org/10.1038/s41577-019-0268-7

Castro-Dopico, T., T.W. Dennison, J.R. Ferdinand, R.J. Mathews, A. Fleming, D. Clift, B.J. Stewart, C. Jing, K. Strongili, L.I. Labzin, et al. 2019. Anticommensal IgG drives intestinal inflammation and type 17 immunity in ulcerative colitis. *Immunity*. 50:1099–1114.e10. https://doi.org/10.1016/j.immuni.2019.02.006

Cerutti, A. 2008. The regulation of IgA class switching. *Nat. Rev. Immunol.* 8:421–434. https://doi.org/10.1038/nri2322

Chen, H., and P.C. Boutros. 2011. VennDiagram: A package for the generation of highly-customizable Venn and euler diagrams in R. *BMC Bioinformatics*. 12:35. https://doi.org/10.1186/1471-2105-12-35

Chen, K., G. Magri, E.K. Grasset, and A. Cerutti. 2020. Rethinking mucosal antibody responses: IgM, IgG and IgD join IgA. *Nat. Rev. Immunol.* 20:427–441. https://doi.org/10.1038/s41577-019-0261-1

De Souza, H.S.P., and C. Fiocchi. 2015. Immunopathogenesis of IBD: Current state of the art. *Nat. Rev. Gastroenterol. Hepatol.* 13:13–27. https://doi.org/10.1038/nrgastro.2015.186

Doron, I., M. Mesko, X.V. Li, T. Kusakabe, I. Leonardi, D.G. Shaw, W.D. Fiers, W.Y. Lin, M. Bialt-DeCelie, E. Román, et al. 2021. Mycobiota-induced IgA antibodies regulate fungal commensalism in the gut and are dysregulated in Crohn's disease. *Nat. Microbiol.* 6:1493–1504. https://doi.org/10.1038/s41564-021-00983-z

Ellebedy, A.H., K.J.L. Jackson, H.T. Kissick, H.I. Nakaya, C.W. Davis, K.M. Roskin, A.K. McElroy, C.M. Oshansky, R. Elbein, S. Thomas, et al. 2016. Defining antigen-specific plasmablast and memory B cell subsets in human blood after viral infection or vaccination. *Nat. Immunol.* 17:1226–1234. https://doi.org/10.1038/ni.3533

Ellebrecht, C.T., E.M. Mukherjee, Q. Zheng, E.J. Choi, S.G. Reddy, X. Mao, and A.S. Payne. 2018. Autoreactive IgG and IgA B cells evolve through

distinct subclass switch pathways in the autoimmune disease pemphigus vulgaris. *Cell Rep.* 24:2370–2380. https://doi.org/10.1016/j.celrep.2018.07.093

Fadlallah, J., H. El Kafsi, D. Sterlin, C. Juste, C. Parizot, K. Dorgham, G. Autaa, D. Gouas, M. Almeida, P. Lepage, et al. 2018. Microbial ecology perturbation in human IgA deficiency. *Sci. Transl. Med.* 10:eaan1217. https://doi.org/10.1126/scitranslmed.aan1217

Fagarasan, S., S. Kawamoto, O. Kanagawa, and K. Suzuki. 2010. Adaptive immune regulation in the gut: T cell–dependent and T cell–independent IgA synthesis. *Annu. Rev. Immunol.* 28:243–273. https://doi.org/10.1146/annurev-immunol-030409-101314

Fenton, T.M., P.B. Jørgensen, K. Niss, S.J.S. Rubin, U.M. Mörbe, L.B. Riis, C. Da Silva, A. Plumb, J. Vandamme, H.L. Jakobsen, et al. 2020. Immune profiling of human gut-associated lymphoid tissue identifies a role for isolated lymphoid follicles in priming of region-specific immunity. *Immunity*. 52:557–570.e6. https://doi.org/10.1016/j.immuni.2020.02.001

Giudicelli, V., D. Chaume, and M.P. Lefranc. 2005. IMGT/GENE-DB: A comprehensive database for human and mouse immunoglobulin and T cell receptor genes. *Nucleic Acids Res.* 33:D256–D261. https://doi.org/10.1093/nar/gki010

Greiff, V., P. Bhat, S.C. Cook, U. Menzel, W. Kang, and S.T. Reddy. 2015. A bioinformatic framework for immune repertoire diversity profiling enables detection of immunological status. *Genome Med.* 7:49. https://doi.org/10.1186/s13073-015-0169-8

Guarner, F., and J.R. Malagelada. 2003. Gut flora in health and disease. *Lancet*. 361:512–519. https://doi.org/10.1016/S0140-6736(03)12489-0

Gupta, N.T., J.A. Vander Heiden, M. Uduman, D. Gadala-Maria, G. Yaari, and S.H. Kleinstein. 2015. Change-O: A toolkit for analyzing large-scale B cell immunoglobulin repertoire sequencing data. *Bioinformatics*. 31:3356–3358. https://doi.org/10.1093/bioinformatics/btv359

Halliley, J.L., C.M. Tipton, J. Liesveld, A.F. Rosenberg, J. Darce, I.V. Gregoretti, L. Popova, D. Kaminiski, C.F. Fucile, I. Albizua, et al. 2015. Long-lived plasma cells are contained within the CD19(−)CD38(hi)CD138(+) subset in human bone marrow. *Immunity*. 43:132–145. https://doi.org/10.1016/j.immuni.2015.06.016

Hapfelmeier, S., M.A.E. Lawson, E. Slack, J.K. Kirundi, M. Stoel, M. Heikenwalder, J. Cahenzli, Y. Velykoredko, M.L. Balmer, K. Endt, et al. 2010. Reversible microbial colonization of germ-free mice reveals the dynamics of IgA immune responses. *Science*. 328:1705–1709. https://doi.org/10.1126/science.1188454

He, B., W. Xu, P.A. Santini, A.D. Polydorides, A. Chiu, J. Estrella, M. Shan, A. Chadburn, V. Villanacci, A. Plebani, et al. 2007. Intestinal bacteria trigger T cell-independent immunoglobulin A(2) class switching by inducing epithelial-cell secretion of the cytokine APRIL. *Immunity*. 26:812–826. https://doi.org/10.1016/j.immuni.2007.04.014

Hendricks, J., A. Visser, P.M. Dammers, J.G.M. Burgerhof, N.A. Bos, and F.G.M. Kroese. 2019. The formation of mutated IgM memory B cells in rat splenic marginal zones is an antigen dependent process. *PLoS One*. 14:e0220933. https://doi.org/10.1371/journal.pone.0220933

Hershberg, U., M. Uduman, M.J. Shlomchik, and S.H. Kleinstein. 2008. Improved methods for detecting selection by mutation analysis of Ig V region sequences. *Int. Immunol.* 20:683–694. https://doi.org/10.1093/intimm/dxn026

Hoehn, K.B., J.S. Turner, F.I. Miller, R. Jiang, O.G. Pybus, A.H. Ellebedy, and S.H. Kleinstein. 2021. Human B cell lineages associated with germinal centers following influenza vaccination are measurably evolving. *Elife*. 10:e70873. https://doi.org/10.7554/eLife.70873

Horns, F., C. Vollmers, D. Croote, S.F. Mackey, G.E. Swan, C.L. Dekker, M.M. Davis, and S.R. Quake. 2016. Lineage tracing of human B cells reveals the in vivo landscape of human antibody class switching. *Elife*. 5:e16578. https://doi.org/10.7554/eLife.16578

Huus, K.E., C. Petersen, and B.B. Finlay. 2021. Diversity and dynamism of IgA-microbiota interactions. *Nat. Rev. Immunol.* 21:514–525. https://doi.org/10.1038/s41577-021-00506-1

Inui, M., S. Hirota, K. Hirano, H. Fujii, A. Sugahara-Tobinai, T. Ishii, H. Harigae, and T. Takai. 2015. Human CD43+ B cells are closely related not only to memory B cells phenotypically but also to plasmablasts developmentally in healthy individuals. *Int. Immunol.* 27:345–355. https://doi.org/10.1093/intimm/dxv009

Islam, K.B., L. Nilsson, P. Sideras, L. Hammarström, and C.I.E. Smith. 1991. TGF-β 1 induces germ-line transcripts of both IgA subclasses in human B lymphocytes. *Int. Immunol.* 3:1099–1106. https://doi.org/10.1093/intimm/3.11.1099

Jackson, M.A., C. Pearson, N.E. Ilott, K.E. Huus, A.N. Hegazy, J. Webber, B.B. Finlay, A.J. Macpherson, F. Powrie, and L.H. Lam. 2021. Accurate identification and quantification of commensal microbiota bound by host immunoglobulins. *Microbiome*. 9:33. https://doi.org/10.1186/s40168-020-00992-w

Jahnsen, F.L., E.S. Bækkevold, J.R. Hov, and O.J. Landsverk. 2018. Do long-lived plasma cells maintain a healthy microbiota in the gut? *Trends Immunol.* 39:196–208. https://doi.org/10.1016/j.it.2017.10.006

Johansen, F.-E., R. Braathen, and P. Brandtzaeg. 2001. The J chain is essential for polymeric Ig receptor-mediated epithelial transport of IgA. *J. Immunol.* 167:5185–5192. https://doi.org/10.4049/jimmunol.167.9.5185

Kaakoush, N.O. 2015. Insights into the role of Erysipelotrichaceae in the human host. *Front. Cell. Infect. Microbiol.* 5:84. https://doi.org/10.3389/fcimb.2015.00084

Kabbert, J., J. Benckert, T. Rollenske, T.C.A. Hitch, T. Clavel, V. Cerovic, H. Wardemann, and O. Pabst. 2020. High microbiota reactivity of adult human intestinal IgA requires somatic mutations. *J. Exp. Med.* 217:e20200275. https://doi.org/10.1084/jem.20200275

Kawamoto, S., T.H. Tran, M. Maruya, K. Suzuki, Y. Doi, Y. Tsutsui, L.M. Kato, and S. Fagarasan. 2012. The inhibitory receptor PD-1 regulates IgA selection and bacterial composition in the gut. *Science*. 336:485–489. https://doi.org/10.1126/science.1217718

Kawamoto, S., M. Maruya, L.M. Kato, W. Suda, K. Atarashi, Y. Doi, Y. Tsutsui, H. Qin, K. Honda, T. Okada, et al. 2014. Foxp3(+) T cells regulate immunoglobulin a selection and facilitate diversification of bacterial species responsible for immune homeostasis. *Immunity*. 41:152–165. https://doi.org/10.1016/j.immuni.2014.05.016

Kett, K., and P. Brandtzaeg. 1987. Local IgA subclass alterations in ulcerative colitis and Crohn's disease of the colon. *Gut*. 28:1013–1021. https://doi.org/10.1136/gut.28.8.1013

Kim, S.V., W.V. Xiang, C. Kwak, Y. Yang, X.W. Lin, M. Ota, U. Sarpel, D.B. Rifkin, R. Xu, and D.R. Littman. 2013. GPR15-mediated homing controls immune homeostasis in the large intestine mucosa. *Science*. 340:1456–1459. https://doi.org/10.1126/science.1237013

King, H.W., N. Orban, J.C. Riches, A.J. Clear, G. Warnes, S.A. Teichmann, and L.K. James. 2021. Single-cell analysis of human B cell maturation predicts how antibody class switching shapes selection dynamics. *Sci. Immunol.* 6:eabe6291. https://doi.org/10.1126/sciimmunol.abe6291

Kitaura, K., H. Yamashita, H. Ayabe, T. Shini, T. Matsutani, and R. Suzuki. 2017. Different somatic hypermutation levels among antibody subclasses disclosed by a new next-generation sequencing-based antibody repertoire analysis. *Front. Immunol.* 8:389. https://doi.org/10.3389/fimmu.2017.00389

Kubinak, J.L., and J.L. Round. 2016. Do antibodies select a healthy microbiota? *Nat. Rev. Immunol.* 16:767–774. https://doi.org/10.1038/nri.2016.114

Landsverk, O.J.B., O. Snir, R.B. Casado, L. Richter, J.E. Mold, P. Réu, R. Horneland, V. Paulsen, S. Yaqub, E.M. Aandahl, et al. 2017. Antibody-secreting plasma cells persist for decades in human intestine. *J. Exp. Med.* 214:309–317. https://doi.org/10.1084/jem.20161590

Lim, T.S., S. Mollova, F. Rubelt, V. Sievert, S. Dübel, H. Lehrach, and Z. Konthur. 2010. V-gene amplification revisited - an optimised procedure for amplification of rearranged human antibody genes of different isotypes. *N. Biotechnol.* 27:108–117. https://doi.org/10.1016/j.nbt.2010.01.001

Lin, M., L. Du, P. Brandtzaeg, and Q. Pan-Hammarström. 2014. IgA subclass switch recombination in human mucosal and systemic immune compartments. *Mucosal Immunol.* 7:511–520. https://doi.org/10.1038/mi.2013.68

Lindner, C., I. Thomsen, B. Wahl, M. Ugur, M.K. Sethi, M. Friedrichsen, A. Smoczek, S. Ott, U. Baumann, S. Suerbaum, et al. 2015. Diversification of memory B cells drives the continuous adaptation of secretory antibodies to gut microbiota. *Nat. Immunol.* 16:880–888. https://doi.org/10.1038/ni.3213

Macpherson, A.J., B. Yilmaz, J.P. Limenitakis, and S.C. Ganal-Vonarburg. 2018. IgA function in relation to the intestinal microbiota. *Annu. Rev. Immunol.* 36:359–381. https://doi.org/10.1146/annurev-immunol-042617-053238

Magri, G., L. Comerma, M. Pybus, J. Sintes, D. Lligé, D. Segura-Garzón, S. Bascones, A. Yeste, E.K. Grasset, C. Gutzeit, et al. 2017. Human secretory IgM emerges from plasma cells clonally related to gut memory B cells and targets highly diverse commensals. *Immunity*. 47:118–134.e8. https://doi.org/10.1016/j.immuni.2017.06.013

Manichanh, C., N. Borruel, F. Casellas, and F. Guarner. 2012. The gut microbiota in IBD. *Nat. Rev. Gastroenterol. Hepatol.* 9:599–608. https://doi.org/10.1038/nrgastro.2012.152

Martin, J.C., C. Chang, G. Boschetti, R. Ungaro, M. Giri, J.A. Grout, K. Gettler, L.S. Chuang, S. Nayar, A.J. Greenstein, et al. 2019. Single-cell analysis of

Crohn's disease lesions identifies a pathogenic cellular module associated with resistance to anti-TNF therapy. *Cell*. 178:1493–1508.e20. https://doi.org/10.1016/j.cell.2019.08.008

Mei, H.E., I. Wirries, D. Frölich, M. Brisslert, C. Giesecke, J.R. Grün, T. Alexander, S. Schmidt, K. Luda, A.A. Kühl, et al. 2015. A unique population of IgG-expressing plasma cells lacking CD19 is enriched in human bone marrow. *Blood*. 125:1739–1748. https://doi.org/10.1182/blood-2014-02-555169

Mora, J.R., and U.H. von Andrian. 2008. Differentiation and homing of IgA-secreting cells. *Mucosal Immunol.* 1:96–109. https://doi.org/10.1038/mi.2007.14

Nakajima, A., A. Vogelzang, M. Maruya, M. Miyajima, M. Murata, A. Son, T. Kuwahara, T. Tsuruyama, S. Yamada, M. Matsuura, et al. 2018. IgA regulates the composition and metabolic function of gut microbiota by promoting symbiosis between bacteria. *J. Exp. Med.* 215:2019–2034. https://doi.org/10.1084/jem.20180427

Neuman, H., J. Arrouasse, M. Kedmi, A. Cerutti, G. Magri, and R. Mehr. 2022. IgTreeZ, A toolkit for immunoglobulin gene lineage tree-based analysis, reveals CDR3s are crucial for selection analysis. *Front. Immunol.* 13: 822834. https://doi.org/10.3389/fimmu.2022.822834

Nilsson, L., P. Grant, I. Larsson, S. Pettersson, and P. Sideras. 1995. The human I α 1 region contains a TGF-β 1 responsive enhancer and a putative recombination hotspot. *Int. Immunol.* 7:1191–1204. https://doi.org/10.1093/intimm/7.8.1191

Nouri, N., and S.H. Kleinstein. 2020. Somatic hypermutation analysis for improved identification of B cell clonal families from next-generation sequencing data. *PLoS Comput. Biol.* 16:e1007977. https://doi.org/10.1371/journal.pcbi.1007977

Nowosad, C.R., L. Mesin, T.B.R. Castro, C. Wichmann, G.P. Donaldson, T. Araki, A. Schiepers, A.A.K. Lockhart, A.M. Bilate, D. Mucida, and G.D. Victora. 2020. Tunable dynamics of B cell selection in gut germinal centres. *Nature*. 588:321–326. https://doi.org/10.1038/s41586-020-2865-9

Pabst, O., and A. Izcue. 2022. Secretory IgA: Controlling the gut microbiota. *Nat. Rev. Gastroenterol. Hepatol.* 19:149–150. https://doi.org/10.1038/s41575-021-00563-w

Pabst, O., and E. Slack. 2020. IgA and the intestinal microbiota: The importance of being specific. *Mucosal Immunol.* 13:12–21. https://doi.org/10.1038/s41385-019-0227-4

Palm, N.W., M.R. de Zoete, T.W. Cullen, N.A. Barry, J. Stefanowski, L. Hao, P.H. Degnan, J. Hu, I. Peter, W. Zhang, et al. 2014. Immunoglobulin A coating identifies colitogenic bacteria in inflammatory bowel disease. *Cell*. 158:1000–1010. https://doi.org/10.1016/j.cell.2014.08.006

Pascal, V., M. Pozuelo, N. Borruel, F. Casellas, D. Campos, A. Santiago, X. Martinez, E. Varela, G. Sarrabayrouse, K. Machiels, et al. 2017. A microbial signature for Crohn's disease. *Gut*. 66:813–822. https://doi.org/10.1136/gutjnl-2016-313235

Phad, G.E., D. Pinto, M. Foglierini, M. Akhmedov, R.L. Rossi, E. Malvicini, A. Cassotta, C.S. Fregni, L. Bruno, F. Sallusto, and A. Lanzavecchia. 2022. Clonal structure, stability and dynamics of human memory B cells and circulating plasmablasts. *Nat. Immunol.* 23:1076–1085. https://doi.org/10.1038/s41590-022-01230-1

Planer, J.D., Y. Peng, A.L. Kau, L.V. Blanton, I.M. Ndao, P.I. Tarr, B.B. Warner, and J.I. Gordon. 2016. Development of the gut microbiota and mucosal IgA responses in twins and gnotobiotic mice. *Nature*. 534:263–266. https://doi.org/10.1038/nature17940

Reboldi, A., T.I. Arnon, L.B. Rodda, A. Atakilit, D. Sheppard, and J.G. Cyster. 2016. Mucosal immunology: IgA production requires B cell interaction with subepithelial dendritic cells in peyer's patches. *Science*. 352: aaf4822. https://doi.org/10.1126/science.aaf4822

Roco, J.A., L. Mesin, S.C. Binder, C. Nefzger, P. Gonzalez-Figueroa, P.F. Canete, J. Ellyard, Q. Shen, P.A. Robert, J. Cappello, et al. 2019. Class-switch recombination occurs infrequently in germinal centers. *Immunity*. 51:337–350.e7. https://doi.org/10.1016/j.immuni.2019.07.001

Rollenske, T., S. Burkhalter, L. Muerner, S. von Gunten, J. Lukasiewicz, H. Wardemann, and A.J. Macpherson. 2021. Parallelism of intestinal secretory IgA shapes functional microbial fitness. *Nature*. 598:657–661. https://doi.org/10.1038/s41586-021-03973-7

Seikrit, C., and O. Pabst. 2021. The immune landscape of IgA induction in the gut. *Semin. Immunopathol.* 43:627–637. https://doi.org/10.1007/s00281-021-00879-4

Shahaf, G., M. Barak, N.S. Zuckerman, N. Swerdlin, M. Gorfine, and R. Mehr. 2008. Antigen-driven selection in germinal centers as reflected by the shape characteristics of immunoglobulin gene lineage trees: A large-scale simulation study. *J. Theor. Biol.* 255:210–222. https://doi.org/10.1016/j.jtbi.2008.08.005

Shapiro, J.M., M.R. de Zoete, N.W. Palm, Y. Laenen, R. Bright, M. Mallette, K. Bu, A.A. Bielecka, F. Xu, A. Hurtado-Lorenzo, et al. 2021. Immunoglobulin A targets a unique subset of the microbiota in inflammatory bowel disease. *Cell Host Microbe*. 29:83–93.e3. https://doi.org/10.1016/j.chom.2020.12.003

Simurina, M., N. De Haan, F. Vu Ckovi, N.A. Kennedy, J. Stambuk, D. Falck, I. Trbojevi C-Akma Ci, F. Clerc, G. Razdorov, A. Khon, et al. 2018. Glycosylation of immunoglobulin G associates with clinical features of inflammatory bowel diseases. *Gastroenterology*. 154:1320–1333.e10. https://doi.org/10.1053/j.gastro.2018.01.002

Sterlin, D., J. Fadlallah, E. Slack, and G. Gorochov. 2019. The antibody/microbiota interface in health and disease. *Mucosal Immunol.* 13:3–11. https://doi.org/10.1038/s41385-019-0192-y

Sterlin, D., J. Fadlallah, O. Adams, C. Fieschi, C. Parizot, K. Dorgham, A. Rajkumar, G. Autaa, H. El-Kafsi, J.L. Charuel, et al. 2020. Human IgA binds a diverse array of commensal bacteria. *J. Exp. Med.* 217:e20181635. https://doi.org/10.1084/jem.20181635

Tiller, T., E. Meffre, S. Yurasov, M. Tsuiji, M.C. Nussenzweig, and H. Wardemann. 2008. Efficient generation of monoclonal antibodies from single human B cells by single cell RT-PCR and expression vector cloning. *J. Immunol. Methods*. 329:112–124. https://doi.org/10.1016/j.jim.2007.09.017

Uzzan, M., J.C. Martin, L. Mesin, A.E. Livanos, T. Castro-Dopico, R. Huang, F. Petralia, G. Magri, S. Kumar, Q. Zhao, et al. 2022. Ulcerative colitis is characterized by a plasmablast-skewed humoral response associated with disease activity. *Nat. Med.* 28:766–779. https://doi.org/10.1038/s41591-022-01680-y

Vander Heiden, J.A., G. Yaari, M. Uduman, J.N.H. Stern, K.C. O'Connor, D.A. Hafler, F. Vigneault, and S.H. Kleinstein. 2014. pRESTO: A toolkit for processing high-throughput sequencing raw reads of lymphocyte receptor repertoires. *Bioinformatics*. 30:1930–1932. https://doi.org/10.1093/bioinformatics/btu138

Wang, Y., L. Liu, D.J. Moore, X. Shen, R.M. Peek, S.A. Acra, H. Li, X. Ren, D.B. Polk, and F. Yan. 2017. An LGG-derived protein promotes IgA production through upregulation of APRIL expression in intestinal epithelial cells. *Mucosal Immunol.* 10:373–384. https://doi.org/10.1038/mi.2016.57

Woof, J.M., and M.W. Russell. 2011. Structure and function relationships in IgA. *Mucosal Immunol.* 4:590–597. https://doi.org/10.1038/mi.2011.39

Wu, Y.-C., D. Kipling, H.S. Leong, V. Martin, A.A. Ademokun, and D.K. Dunn-Walters. 2010. High-throughput immunoglobulin repertoire analysis distinguishes between human IgM memory and switched memory B-cell populations. *Blood*. 116:1070–1078. https://doi.org/10.1182/blood-2010-03-275859

Ye, J., N. Ma, T.L. Madden, and J.M. Ostell. 2013. IgBLAST: An immunoglobulin variable domain sequence analysis tool. *Nucleic Acids Res.* 41: W34–W340. https://doi.org/10.1093/nar/gkt382

Supplemental material

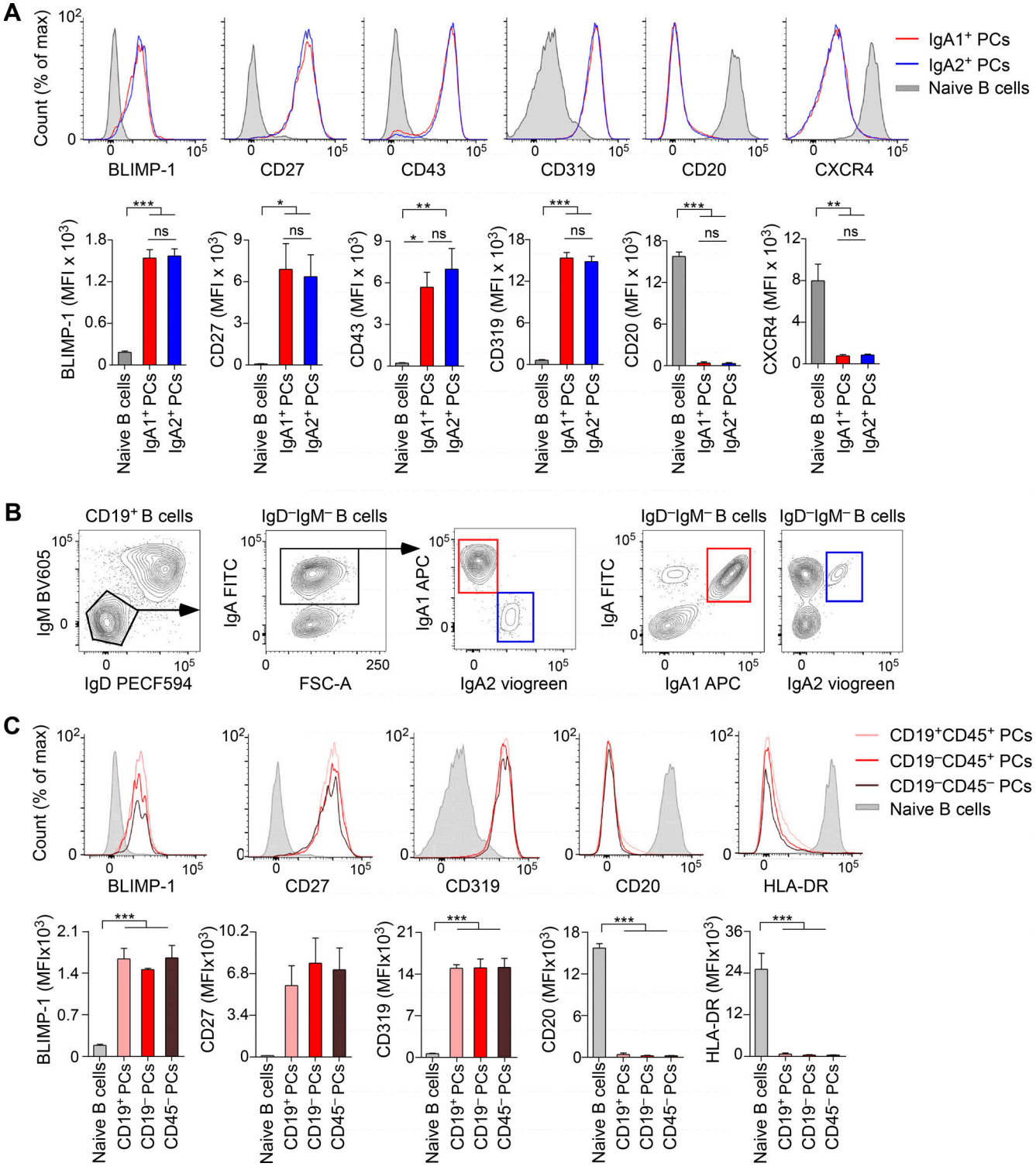

Figure S1. **Human Intestinal IgA1⁺ and IgA2⁺ PCs express a comparable phenotype and canonical PC properties. (A)** FCA and MFI of intracellular BLIMP-1 or surface CD27, CD43, CD319, CD20, and CXCR4 in intestinal naïve B cells, IgA1⁺ PCs and IgA2⁺ PCs of a representative adult donor (top panels) or at least three donors (bottom panels). **(B)** FCA of IgM, IgD, IgA, IgA1, and IgA2 was performed on circulating viable DAPI⁻CD19⁺ B cells to validate the specificity of the staining to IgA2 subclass. IgA1⁺ cells were defined as IgA⁺ IgA2⁻, whereas IgA2⁺ cells were defined as IgA⁺ IgA2⁺. **(C)** FCA of intracellular BLIMP-1 and surface CD27, CD319, CD20, or HLA-DR in control naive B cells (gray) as well as CD19⁺CD45⁺ (or CD19⁺), CD19⁻CD45⁺ (or CD19⁻), and CD19⁻CD45⁻ (or CD45⁻) subsets of total viable DAPI⁻ CD10⁻CD38^{hi} IgA⁺ PCs from the terminal ileum or ascending colon of a representative adult donor (top panels) or at least three donors (bottom panels). Data show one of at least three experiments yielding similar results (B) or summarize results from three or more donors (A and C). Results are presented as mean ± SEM; one-way ANOVA with Tukey's post-hoc test. *P < 0.05, **P < 0.01, ***P < 0.001.

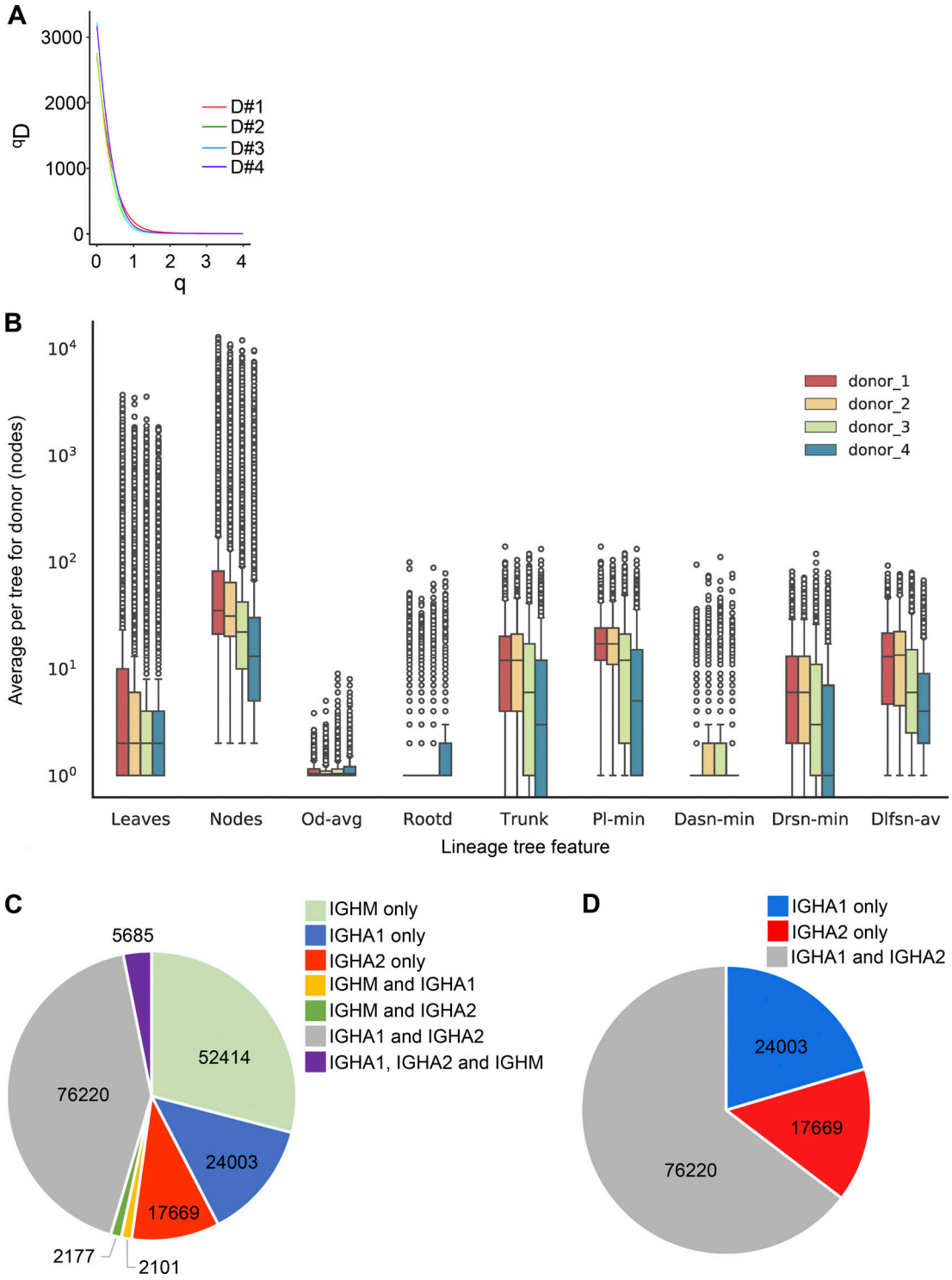

Figure S2. **Repertoire and lineage tree features. (A)** Diversity profiles showing the calculated repertoire diversity measure ^{q}D in each donor versus the diversity order q. For q = 1, ^{q}D is the "species richness," i.e., the number of species—or clones—observed in the repertoire. For q = 2, ^{q}D is Shannon's information, which also accounts for species abundance (clone sizes here). Higher orders give more weight to the larger clones by using higher powers of clone sizes. 34,000 clones were sampled from each repertoire, after excluding naïve B cells to avoid biases due to repertoire size. **(B)** Tree topological features for D#1 (red), D#2 (orange), D#3 (green), and D#4 (blue). All lengths/distances are measured in the number of tree nodes. Minima, maxima, and averages are calculated per tree, then averaged per donor. Features shown are the following. Leaves, total number of leaves in the tree; Nodes, total number of nodes in the tree; Od-avg, the average outgoing degree of all nodes; Rootd, root outgoing degree (the number of branches going out of the root node); Trunk, trunk length; Pl-min, the minimum path length from the root to a leaf, including the trunk; Dasn-min, the minimum distance between adjacent split nodes ("forks"), i.e., an inverse measure of tree branching; Drsn-min, the minimum distance from the root to any split node; Dlfsn-avg, the average distance from a leaf node (branch end) back to the first split node. **(C and D)** Pie chart and numbers of lineage trees containing sequences of the indicated isotypes (C) or only of IgA isotype (D) in all four donors.

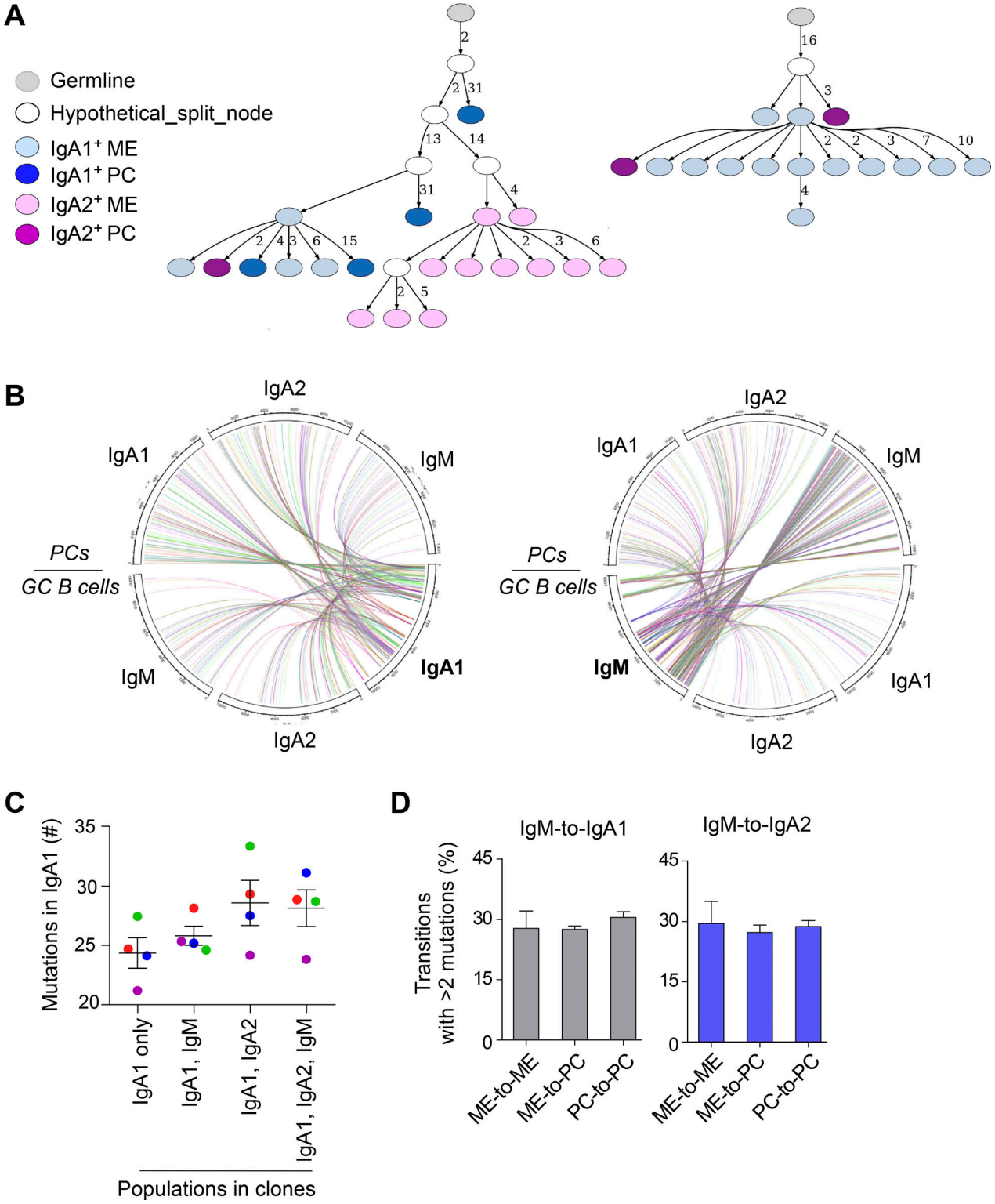

Figure S3. **Some human intestinal IgA2 may derive from both GC and extra-GC IgA1⁺ B cells. (A)** Lineage trees from a representative donor. Color codes correspond to specific B cell and PC subsets. Trees were colored using a custom script and drawn using a local version of Graphviz. ME, memory; IL, ileum. Numbers indicate mutations; edges with no attached number indicate one mutation. **(B)** Circos plots from donor D#3 depicting clonal relationships between GC B cells and PCs and expressing IgA1 (left) or IgM (right) as isotype of reference (shown in bold). **(C)** Average numbers of mutations of IgA1 sequences in clones sharing other antibody classes or subclasses as indicated. D#1, blue; D#2, red; D#3, green; D#4, purple. **(D)** Frequencies of transitions from IgM to IgA1 (left) or from IgM to IgA2 (right) with >2 mutations generated during ME B cell-to-ME B cell, ME B cell-to-PC or PC-to-PC maturation events. Results are presented as mean ± SEM.

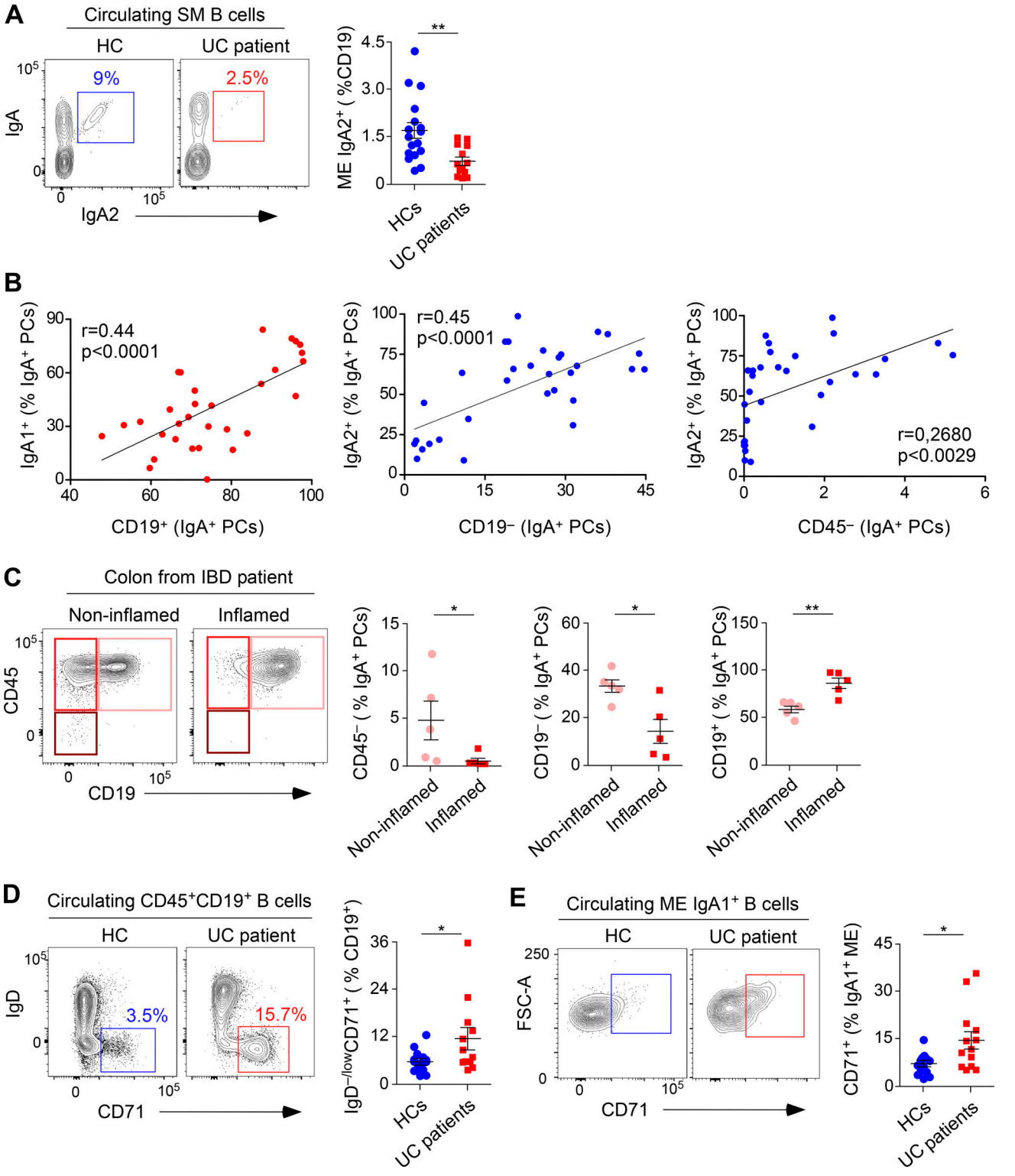

Figure S4. **Human gut inflammation induces expansion of mucosal IgA1⁺ PB along with depletion of mucosal and circulating IgA2⁺ memory B cells and PCs. (A)** FCA of IgA and IgA2 expression on total circulating switched memory (SM) B cells and frequencies of IgA2⁺ memory (ME) B cells from total circulating CD19⁺ B cells of HCs and UC patients. **(B)** Pearson's correlations between the frequency of intestinal IgA1⁺ or IgA2⁺ PCs and the frequency of CD19⁺, CD19⁻, and CD45⁻ IgA⁺ PCs. **(C)** Representative FCA (left plots) and frequency of CD19⁺, CD19⁻, and CD45⁻ PCs (right graphs) on colonic LP IgA⁺ PCs from both inflamed and non-inflamed gut segments from UC patients (n = 5). **(D)** FCA of IgD and CD71 expression on total circulating CD19⁺ B cells and frequencies of recently activated IgD^{low}CD71⁺ B cells out of total circulating CD19⁺ B cells in HCs and UC patients. **(E)** Representative FCA of CD71 expression in circulating IgA⁺ memory B cells and frequencies of recently activated CD71⁺ B cells out of total IgA1⁺ memory B cells from HCs and UC patients. Data show one of more than three experiments yielding similar results (A left, C left, and D left) or summarize results from 17 HCs to 13 UC patients (A right, B, D, and E) or 5 UC patients (C). Error bars, SEM; Mann–Whitney U test (A, D, and E), Wilcoxon matched paired test (C). *P < 0.05, **P < 0.01.

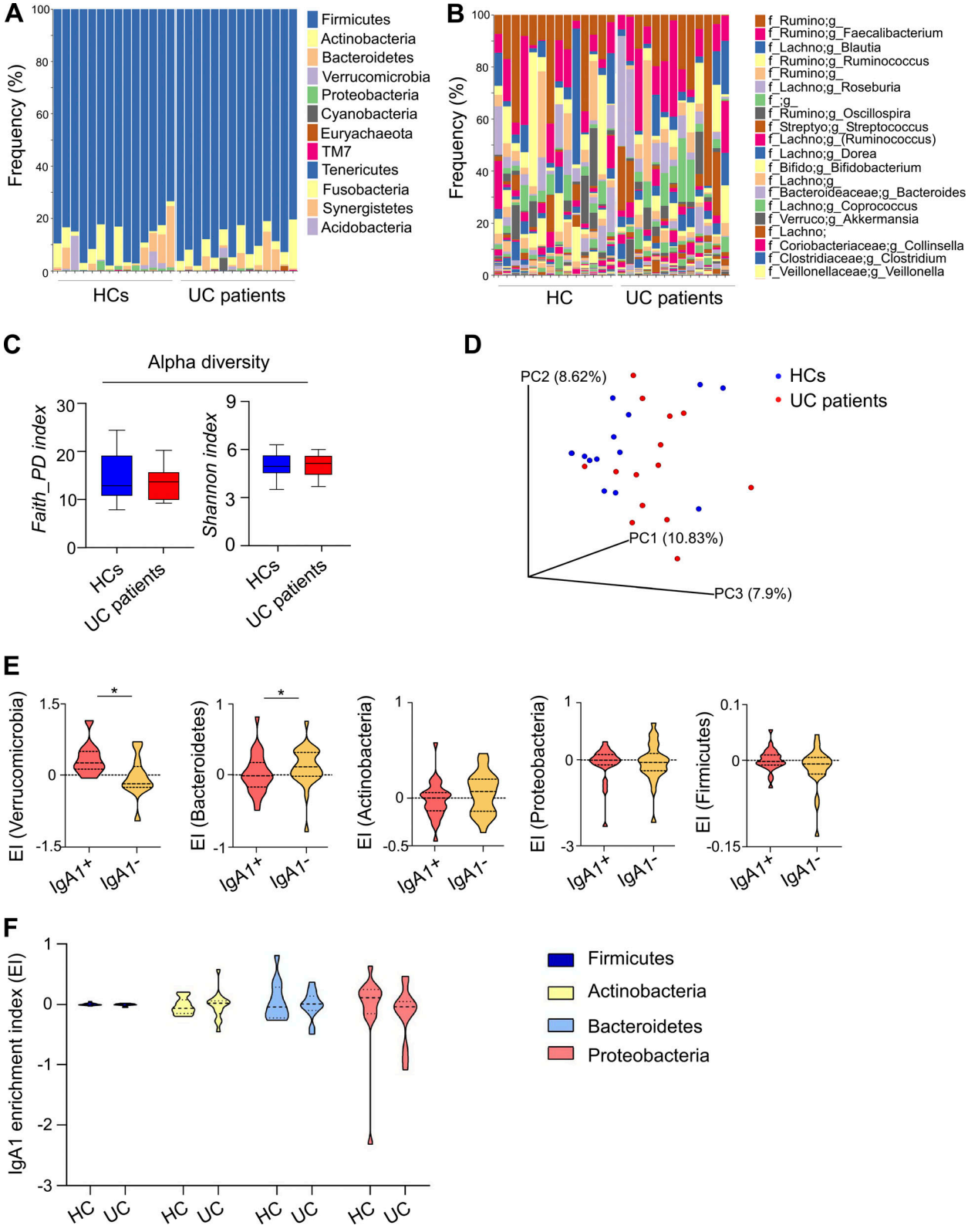

Figure S5. **The fecal bacterial MB from HCs and UC patients does not show major compositional differences. (A and B)** Frequencies of phyla (A) and genera (B) in fecal bacterial inputs obtained from fecal MB of HCs and UC patients as in Fig. 7 H (left plot). **(C)** Phylogenetic richness (left), shown as Faith_PD index, and species diversity (right), shown as Shannon index, of fecal MB input samples obtained as depicted in Fig. 7 H (left plot) from HCs and UC patients. **(D)** PCA shows the β diversity of fecal MB input samples from HCs and UC patients. **(E)** EI for *Firmicutes*, *Bacteroidetes*, *Actinobacteria*, *Proteobacteria*, and *Verrucomicrobia* in bacterial IgA1$^+$ and IgA1$^-$ fractions obtained from the fecal MB of HCs and UC patients as in Fig. 7 H (left plot). **(F)** IgA1 EI in *Firmicutes*, *Actinobacteria*, *Bacteroidetes*, and *Proteobacteria* in bacterial fractions obtained from the fecal MB of HCs and UC patients as in Fig. 7 H (left plot). Data summarize the results of 14 HC and 14 UC. Error bars, SEM (C); two-tailed Mann–Whitney *U* test (C, E, and F); *P < 0.05.

Provided online are Table S1, Table S2, Table S3, Table S4, Table S5, Table S6, Table S7, and Table S8. Tables S1 shows tissue and blood samples analyzed by flow cytometry (FC) or immunofluorescence (IF) microscopy. Table S2 shows fecal samples. Table S3 shows intestinal mucus samples. Table S4 shows antibodies used for flow cytometry, immunofluorescence microscopy, and ELISA. Table S5 shows populations and number of cells sorted for Ig gene repertoire analysis. Table S6 shows primers used for next-generation sequencing. Table S7 shows the number of IGHV sequences that have passed each stage of preprocessing. Table S8 shows the number of IGHV sequences that have passed IMGT and filtering for functional sequences as well as the number of clones and threshold for their assignment.